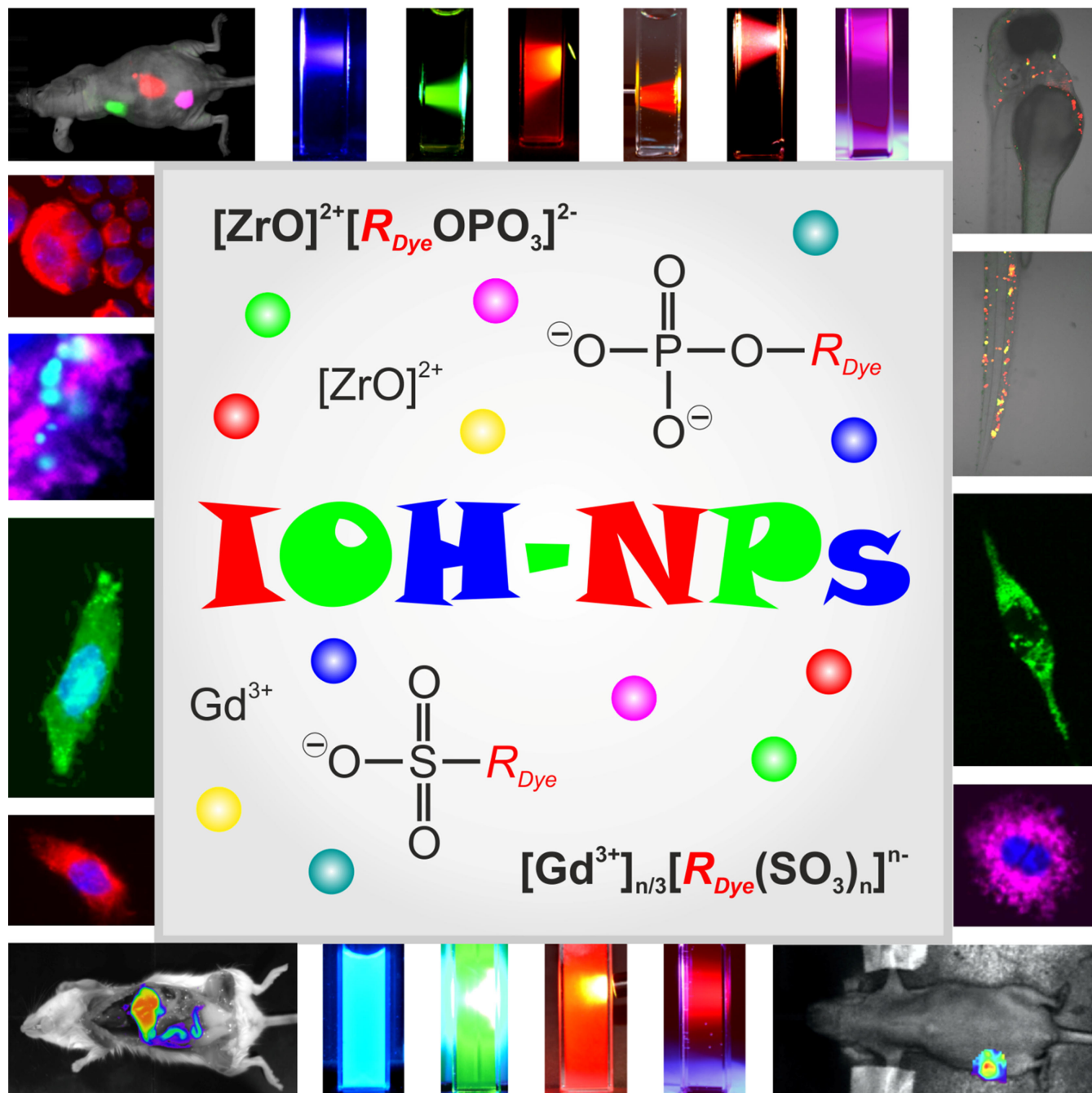


## Hybrid Materials

# Fluorescent Inorganic-Organic Hybrid Nanoparticles

B. Lilli Neumeier,<sup>[a]</sup> Mikhail Khorenko,<sup>[a]</sup> Frauke Alves,<sup>[b]</sup> Oliver Goldmann,<sup>[c]</sup> Joanna Napp,<sup>[b]</sup> Ute Schepers,<sup>[d]</sup> Holger M. Reichardt,<sup>[e]</sup> and Claus Feldmann<sup>\*[a]</sup>

*Dedicated to Professor Bernt Krebs on the occasion of his 80<sup>th</sup> birthday*



**Abstract:** Inorganic-organic hybrid nanoparticles (IOH-NPs) with a general composition  $[\text{ZrO}]^{2+}[\text{R}_{\text{Dye}}\text{OPO}_3]^{2-}$ ,  $[\text{Ln}]^{3+}_{n/3}[\text{R}_{\text{Dye}}(\text{SO}_3)_n]^{n-}$ ,  $[\text{Ln}(\text{OH})]^{2+}_{n/2}[\text{R}_{\text{Dye}}(\text{SO}_3)_n]^{n-}$ , or  $[\text{LnO}]^+_{n/3}[\text{R}_{\text{Dye}}(\text{SO}_3)_n]^{n-}$  (Ln: lanthanide) are a novel class of nanomaterials for fluorescence detection and optical imaging. IOH-NPs are characterized by an extremely high load of the fluorescent dye (70–85 wt-%), high photochemical stability, straightforward aqueous synthesis, low material complexity, intense

emission and high cell uptake at low toxicity. Besides full-color emission, IOH-NPs are suitable for multimodal imaging, singlet-oxygen generation as well as drug delivery and drug release. This focus review presents the material concept of the IOH-NPs as well as their synthesis and characterization. Their characteristic features are illustrated by selected *in vitro* and *in vivo* studies to initiate application in biology and medicine.

## 1. Introduction

Medicine and molecular biology belong to the most fascinating and most challenging areas of nanoparticle application.<sup>[1]</sup> Here, nanoparticles generally address two different subjects: Diagnosis and therapy.<sup>[2]</sup> Aiming at diagnosis, nanoparticles can serve as contrast agents for all kinds of imaging techniques including optical imaging (OI), photoacoustic imaging (PAI), magnetic resonance imaging (MRI), ultrasonic imaging (US), computed tomography (CT), scintigraphy (SC), or positron emission tomography (PET).<sup>[3]</sup> In regard of therapy, nanoparticles are promising carriers for drug delivery and release. For instance, this includes analgesic, anti-tumor, anti-inflammatory, antibiotic or antiviral agents and allows to address a wide range of disease patterns.<sup>[4]</sup>

In the recent decade, imaging techniques have made tremendous progress due to the technological development of imaging devices (i.e. hardware), enormous advancements in the evaluation and processing of great amounts of data (i.e. software),<sup>[3]</sup> and finally due to powerful additives – so-called contrast agents – that allow enhancing contrast, significance, reliability and specificity.<sup>[3]</sup> Whereas the first areas belong to

engineering and computer science, contrast agents are the domain of natural science. In general, the role of contrast agents is to visualize whole organisms, specific organs and tissue, or even single cells in animals (e.g., mice, rats) and humans.<sup>[1,5]</sup> Certain contrast agents are long used in the clinics for almost all imaging techniques.<sup>[3,5]</sup> Prominent examples comprise, for instance, Gd complexes for MRI,<sup>[6]</sup> BaSO<sub>4</sub> for CT,<sup>[7]</sup> or <sup>99</sup>Tc and <sup>131</sup>I compounds in nuclear medicine.<sup>[8]</sup>

Imaging techniques are widely used in clinical practice and suitable for obtaining detailed information at high resolution. However, they also require cumbersome equipment and time-consuming data acquisition.<sup>[3]</sup> In this regard, especially OI offers new opportunities for non-invasive diagnosis and *in vivo* observation of complex vital functions.<sup>[9]</sup> OI is fast and easy to operate and requires comparably cheap equipment as well as uncomplex data manipulation. Tremendous efforts have been already made to unveil organ distribution with deep tissue information and to improve optical contrast and spatial resolution. However, OI essentially requires suitable fluorescent contrast agents. Even more interesting than single-modality contrast agents is the option of multimodal detection to combine the specific assets of different imaging techniques for the visualization of various types of tissue on different scales of resolution, for the translation from preclinical to clinical imaging, or the translation of preoperational to intraoperative imaging.<sup>[10]</sup>

This review is specifically focused on fluorescent nanoparticles as powerful tags for fluorescence detection and OI. In general, various requirements are prerequisite to contrast agents for any application in basic medical research and life sciences, including: *i*) Low toxicity and sufficient biocompatibility; *ii*) Easy detectability with standard hardware equipment; *iii*) Highly specific signals to prevent optical overlap with autofluorescence from cells and tissue; *iv*) Deep tissue penetration of the irradiation used for excitation and emission; *v*) Straightforward synthesis of contrast agents with low material complexity. In this regard, three types of fluorescent nanoparticles have been yet applied most often: *i*) Semiconductor-type quantum dots (Q-dots),<sup>[11]</sup> *ii*) Up-converting nanoparticles,<sup>[12]</sup> *iii*) Immobilized organic dyes.<sup>[13]</sup>

Aiming at fluorescent nanoparticles, Q-dots beyond doubt represent the most prominent and most widely applied class of inorganic nanoparticles.<sup>[11]</sup> They are designated by unrivalled brightness, intense size-depending emission, likewise in the UV to IR spectral regime, superior photostability, and low photo-

[a] B. L. Neumeier, M. Khorenko, Prof. Dr. C. Feldmann  
Institute of Inorganic Chemistry  
Karlsruhe Institute of Technology (KIT)  
Engesserstraße 15, 76131 Karlsruhe, Germany  
E-mail: claus.feldmann@kit.edu

[b] Prof. Dr. F. Alves, Dr. J. Napp  
Translational Molecular Imaging  
Max-Planck-Institute for Experimental Medicine  
Hermann-Rein-Strasse 3, 37075 Göttingen, Germany

[c] Dr. O. Goldmann  
Helmholtz-Center of Infection Research  
Inhoffenstraße 7, 38124 Braunschweig, Germany

[d] Prof. Dr. U. Schepers  
Institute of Toxicology and Genetics  
Karlsruhe Institute of Technology (KIT)  
Hermann-von-Helmholtz-Platz 1, 76344 Eggenstein-Leopoldshafen, Germany

[e] Prof. Dr. H. M. Reichardt  
Institute for Cellular and Molecular Immunology  
University Medical Center Göttingen (UMG)  
Humboldtallee 34, 37073 Göttingen, Germany

Supporting information for this article is available on the WWW under <https://doi.org/10.1002/cnma.201800310>

© 2018 The Authors. Published by Wiley-VCH Verlag GmbH & Co. KGaA. This is an open access article under the terms of the Creative Commons Attribution Non-Commercial NoDerivs License, which permits use and distribution in any medium, provided the original work is properly cited, the use is non-commercial and no modifications or adaptations are made.

bleaching.<sup>[14]</sup> Since the emission of Q-dots relates to a quantum-confinement effect – i.e. a size-depending band gap,

and thus, a size-depending emission – precise size control is essential to guarantee the quantum-confinement effect (i.e.

**B. Lilli Neumeier** studied chemistry at the Karlsruhe Institute of Technology (KIT). She did her bachelor's thesis in Polymer Science in 2013 and received her master's degree in 2015. She is currently a PhD student in Claus Feldmann's group at the Institute of Inorganic Chemistry, KIT. Her research includes novel inorganic-organic hybrid nanomaterials for medical application.



**Mikhail Khorenko** studied molecular science at the University Erlangen-Nuremberg (Germany, 2011–2016) and completed his master thesis at the Imperial College London (UK, 2016). Since October 2016 he is a PhD student in Claus Feldmann's group at the Karlsruhe Institute of Technology (Germany). His research interests focus on the synthesis of novel multimodal inorganic-organic hybrid nanoparticles for biomedical application.



**Frauke Alves** studied medicine at the University of Göttingen. In 2009, she received her professorship in Internal Medicine. As a clinician she developed a thorough bench to bedside approach in the cancer field by heading a tandem research group at the University Medicine Center (Dept. of Hematology and Medical Oncology and Institute of Diagnostic and Interventional Radiology) and the Max-Planck-Institute for Experimental Medicine, Göttingen. The focus of her "Translational Imaging Group" is the investigation of mechanisms of tumor progression, angiogenesis and inflammation as well as the development of novel therapeutic approaches and diagnostic tools in nanomedicine and oncology.



**Oliver Goldmann** studied biology at the Technical University of Braunschweig and did his doctorate on host genetic influence on infection diseases caused by the human pathogen *Streptococcus pyogenes* in the department of microbial pathogenesis (Singh Chhatwal) at the German Research Centre of Biotechnology, Braunschweig. He continued his work on microbial pathogenesis and the influence of host genetic on bacterial infections in the Infection Immunology Group (Eva Medina) at the Helmholtz Center for Infection Research (HZI, Braunschweig). His research interests are focused on bacterial persistence and host pathogen interactions of Gram-positive cocci.



**Joanna Napp** studied biology at the Nicolaus Copernicus University in Torun, Poland. She did her PhD at the Max-Planck-Institute (MPI) of Experimental Medicine and the European Neuroscience Institute in Göttingen. In 2006, she joined the Translational Molecular Imaging Group of Frauke Alves, with a combined position at the University Medical Center Göttingen (UMG) and at the MPI in Göttingen. In 2015, she started her junior research group Image-based Nanotherapy and Diagnostics at the UMG, supported with a guest-scientist position at the MPI. She has specialized in the *in vivo* imaging of animal disease models, particularly focusing on development and evaluation of novel tumor therapies.



**Ute Schepers** studied chemistry (University of Bonn) and did her doctorate in Biochemistry of brain diseases under Konrad Sandhoff. After post-doctoral studies with Tom Kirchhausen (Harvard Medical School, Boston), she started her junior group at the LIMES Institute in Bonn on organ-targeted drug delivery. In 2009, she became group leader at the Karlsruhe Institute of Technology (KIT), where she habilitated in 2011. In 2015, she was appointed at KIT as leading scientist and received a professorship for Chemical Biology and Biochemistry. Her research interests address organ-targeted drug delivery.



**Holger M. Reichardt** studied biochemistry in Germany (University of Tübingen) and Switzerland (University of Fribourg) and did his doctorate in molecular biology at the German Cancer Research Center (DKFZ) in Heidelberg. After post-doctoral training in the laboratories of Günther Schütz (DKFZ) and John Mullins (University of Edinburgh), he became Professor of Molecular Immunology at the University of Würzburg, where he worked on T cells and macrophages and developed new techniques to genetically manipulate the rat genome using lentiviruses and RNA interference. In 2007, he was appointed Professor of Experimental Immunology at the University of Göttingen. The main focus of his current research is the pathomechanism of chronic inflammatory diseases and the design of new therapeutic concepts and improved immunosuppressive strategies.



**Claus Feldmann** studied chemistry (University of Bonn) and did his doctorate in solid-state chemistry under Martin Jansen. After post-doctoral studies with Hans-Georg von Schnering (Max Planck Institute of Solid-State Research, Stuttgart), he moved to industry (Philips Research Laboratories, Aachen/Eindhoven), where he was engaged in luminescent materials. Simultaneously, he habilitated at the RWTH Aachen on nanomaterials. In 2003, he was appointed at the University of Karlsruhe, the present Karlsruhe Institute of Technology. His research interests address solid-state chemistry and functional nanomaterials.



mean particle diameter  $< 10$  nm) and the color purity of emission (i.e. maximum deviation from the mean diameter  $\pm 0.5$  nm).<sup>[15]</sup> Moreover, high crystallinity and high purity are necessary to exclude defect-driven loss processes. The latter requirement also demands core-shell structures (e.g. CdSe@ZnS) with a luminescent core (e.g. CdSe) that is coated by a non-luminescent shell (e.g. ZnS) to eliminate the solid-to-liquid surface of the luminescent core.<sup>[16]</sup> The above requirements – size control, low defect level, core-shell structure – lead to high efforts for chemical synthesis. The applicability of Q-dots, finally, suffers from additional inherent drawbacks such as harmful elements (e.g. Cd<sup>2+</sup>), sensitivity to hydrolysis, and the hydrophobic properties of the as-prepared material (e.g. due to alkyl-terminated surfaces).<sup>[17]</sup> All in all, advanced strategies of synthesis and surface conditioning are needed to obtain state-of-the-art water-dispersible core-shell Q-dots showing intense emission.<sup>[18]</sup> As an alternative class of fluorescent nanoparticles, moreover, carbon dots (C-dots) came up recently and turned out as very promising due to their improved biocompatibility.<sup>[19]</sup>

Similar demands regarding crystallinity, purity, and surface conditioning with core-shell structures also apply to up-converting nanoparticles (e.g. NaYF<sub>4</sub>:Er,Yb@NaYF<sub>4</sub>) to avoid all kinds of defects, which otherwise reduce the emission intensity.<sup>[12]</sup> Up-conversion – meaning the absorption of two or more photons of lower energy (e.g. IR) followed by the emission of one photon at higher energy (e.g. green) – is established by photon-cascade processes on the precisely defined energy levels of rare-earth-metal ions (e.g., Er<sup>3+</sup>, Yb<sup>3+</sup>).<sup>[20]</sup> Up-conversion-based fluorescence guarantees low background and excellent tissue penetration. On the other hand, up-conversion materials suffer from poor absorption and high photon density. The latter is needed for sufficient excitation (e.g. by monochromatic laser light) of the quantum-mechanically forbidden *f-f* transitions on rare-earth-metal ions.

Besides inorganic nanoparticles, such as Q-dots and up-converting materials, fluorescent organic dyes in aqueous solution are, of course, most often used as tags for fluorescence detection and optical imaging.<sup>[13]</sup> Thus, a great number of fluorescent dyes showing emission from the blue to the infrared spectral regime has been discovered since the beginning of fluorescence microscopy in the early 20<sup>th</sup> century to analyze all kinds of biological probes.<sup>[21]</sup> However, fluorescent organic dyes often do not meet the demands on high emission intensity, sufficient photostability, and chemical resistance under the conditions of investigation.<sup>[29,22]</sup> In particular, low intensity and rapid photobleaching are severe limitations of many fluorescent organic dyes. To evade these intrinsic weaknesses, fluorescent organic dyes – most often including derivatives of rhodamine, cyanine, squaraine, boron-dipyrromethene, porphyrin, phthalocyanine, etc.<sup>[23]</sup> – were attached to or encapsulated in inorganic matrices (e.g., silica, calcium phosphate),<sup>[24]</sup> metalorganic frameworks and coordination polymers,<sup>[25]</sup> organic polymers (e.g., polyglycolic acid/PGA, polylactic acid/PLA, poly(lactic-co-glycolic) acid/PLGA, polycaprolactone/PCL, chitosan),<sup>[13a,26]</sup> as well as liposomes and dendrimers.<sup>[27]</sup> However, surface-attached dyes hold the risk of abrasive debonding. Encapsulation of fluorescent organic dyes in a

matrix, on the other hand, is typically performed via micro-emulsion techniques, which limits the amount of available material.<sup>[28]</sup> Moreover, the concentration of the fluorescent dye in relation to the inert matrix is usually low ( $\leq 5$  wt-%). The limited number of fluorescent centers per nanoparticle volume, however, reduces the emission intensity and increases the threat of photobleaching.

Although fascinating chemical compositions and material structures of fluorescent nanoparticles were realized, aspects such as the emission intensity, photostability, biocompatibility, or biodegradability still need further improvement. The complexity and great number of constituents of certain nanoparticle architectures, in fact, can be a limitation in itself since synthesis and material are becoming more and more complex and expensive. Aiming at medical application, furthermore, all individual constituents as well as all their combinations might need clinical approval.<sup>[29]</sup> Based on the above discussed state-of-the-art, we present inorganic-organic hybrid nanoparticles (IOH-NPs) as a novel concept and class of fluorescent nanoparticles for biomedical issues. We have explored these IOH-NPs since 2008,<sup>[30]</sup> with the intention to identify uncomplex, low-cost nanoparticles showing intense emission and high biocompatibility.

## 2. Fluorescent Inorganic-Organic Hybrid Nanoparticles (IOH-NPs)

The concept of the IOH-NPs is illustrated with phosphate-based IOH-NPs and sulfonate-based IOH-NPs as examples. This includes the chemical synthesis, the material composition as well as the luminescence properties with the specific focus on biomedical application.

### 2.1. Material Concept

Aiming at uncomplex, low-cost nanoparticles for biomedical use, we intended to perform the synthesis in water only, since the addressed area of application – for obvious reasons – is limited to water. Consequently, the aspired nanoparticles need to be insoluble in water. In terms of biocompatibility, phosphates seemed reasonable as they are essential for the energy metabolism of almost all cells.<sup>[31]</sup> In this regard, the most insoluble metal phosphate in water is zirconium phosphate, which is well-known in qualitative analysis to prove the presence either of zirconium or phosphate.<sup>[32]</sup> The precipitation is highly indicative since zirconium phosphate is the only insoluble metal phosphate even in hydrochloric acid at low pH (i.e. pH  $\leq 2$ ).

Although the qualitative test reaction is described in many textbooks, the chemical composition of the aqueous precipitate at room temperature is still not clear. Typically, the composition is denoted as Zr<sub>3</sub>(PO<sub>4</sub>)<sub>4</sub> or Zr(HPO<sub>4</sub>)<sub>2</sub> × H<sub>2</sub>O.<sup>[32,33]</sup> With aqueous conditions at room temperature and at moderate pH (4 to 9), in fact, neither Zr<sup>4+</sup> nor PO<sub>4</sub><sup>3-</sup> are likely as dissolved species due

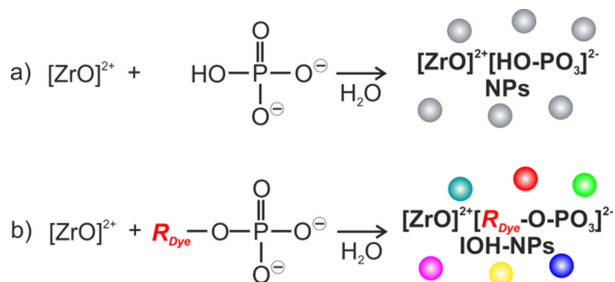


**Figure 1.** Scheme illustrating the synthesis of: a)  $[ZrO]^{2+}[HPO_4]^{2-}$  NPs and b) fluorescent inorganic-organic hybrid nanoparticles (IOH-NPs) with a general composition  $[ZrO]^{2+}[R_{Dye}OPO_3]^{2-}$ .

to their high acidity or alkalinity, respectively. The expected species rather are  $[ZrO]^{2+}$  and  $[HPO_4]^{2-}$  or  $[H_2PO_4]^-$ . Aiming at nanoparticles, a composition  $[ZrO]^{2+}[HPO_4]^{2-}$  is indeed formed upon injection of an aqueous solution of  $ZrOCl_2$  into an aqueous solution of  $Na_2(HPO_4)$  (Figure 1a). It needs to be noted that  $[ZrO]^{2+}[HPO_4]^{2-}$  – similar to all IOH-NPs presented in the following – is amorphous and does not show any Bragg peak. This complicates the determination of composition and structure, hence requiring different independent tools to prove the adopted composition (e.g. Zr:P ratio of  $[ZrO]^{2+}[HPO_4]^{2-}$  determined to 1:1; see 2.4 for details).

Although not showing any luminescence,  $[ZrO]^{2+}[HPO_4]^{2-}$  is the initial point of all IOH-NPs and the origin of a platform of compounds with different compositions.<sup>[34]</sup> To obtain fluorescent IOH-NPs, the simple hydrogen phosphate anion is replaced by a phosphate with a fluorescent organic dye ( $R_{Dye}$ ) bound via a P–O–C ester bond, resulting in a general composition  $[ZrO]^{2+}[R_{Dye}OPO_3]^{2-}$  (Figure 1b).<sup>[34,35]</sup> With this composition, it is obvious that  $R_{Dye}$ , in principle, can comprise a great number of different fluorescent dyes. Essentially, the fluorescent organic dye needs to contain a phosphate functionality to obtain insoluble nanoparticles in water.<sup>[34,35]</sup>

Phosphate-based IOH-NPs  $[ZrO]^{2+}[R_{Dye}OPO_3]^{2-}$  are composed of  $[ZrO]^{2+}$  as an inorganic cation and  $[R_{Dye}OPO_3]^{2-}$  as a fluorescent organic anion.<sup>[36]</sup> Due to charge neutrality, cation and anion are available in 1:1 ratio (in the case of identical charges) and in molar quantities. Such saline composition is similar to simple sodium chloride that consists of equimolar amounts of  $Na^+$  cations and  $Cl^-$  anions. The saline composition also accounts for a specific advantage of the IOH-NPs, which is an unprecedentedly high dye load (70–85 wt-%). Due to the intermixing of the inorganic part (the cation) and the organic part (the anion) on the molecular level, the nanoparticles are designated as “inorganic-organic hybrid nanoparticles”, according to the Latin origin: “*hybrid*”: crossbreed.<sup>[34,35]</sup>

The predominant role of  $[ZrO]^{2+}$  in the IOH-NPs is to guarantee their insolubility in water, which is prerequisite for obtaining nanoparticles as well as for the intended water-limited biomedical application.<sup>[34,35]</sup> A comparable approach was yet only reported for bisphosphonates, which serve as organic bridging ligands in coordination polymers.<sup>[25b,37]</sup> Zirconium as a metal cation is known for its low toxicity and has been clinically approved in the US and the EU, for instance, in the form of

sodium zirconium cyclosilicate (*Lokelma*, AstraZeneca) for the treatment of hyperkalemia<sup>[38]</sup> or in the case of different zirconium complexes as antiperspirants.<sup>[39]</sup> The fluorescent organic anion  $[R_{Dye}OPO_3]^{2-}$  entails the fluorescence features of the IOH-NPs.<sup>[34,35]</sup> In regard of the above considerations,  $[ZrO]^{2+}[R_{Dye}OPO_3]^{2-}$  IOH-NPs already offer the following advantages: *i*) Uncomplex aqueous synthesis; *ii*) Low material complexity; *iii*) High dye load leading to intense emission; *iv*) Wide variability of fluorescent organic anions.

## 2.2. Phosphate-based IOH-NPs

Phosphate-based IOH-NPs with a general chemical composition  $[ZrO]^{2+}[R_{Dye}OPO_3]^{2-}$  are here introduced with the exemplary system  $[ZrO]^{2+}[(HPO_4)_{1-x}(FMN)_x]^{2-}$  ( $x=0-1$ ) containing the inorganic cation  $[ZrO]^{2+}$  as well as the anions  $[HPO_4]^{2-}$  and  $[FMN]^{2-}$ .<sup>[34]</sup> FMN represents the fluorescent organic anion flavin mononucleotide and is a derivative of vitamin B<sub>2</sub> (Figure 2a).<sup>[40]</sup>

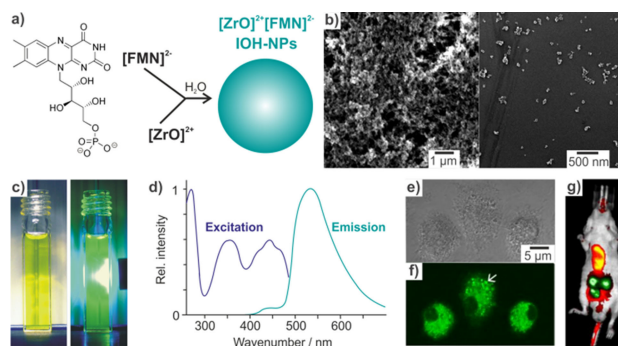


**Figure 2.**  $[ZrO]^{2+}[FMN]^{2-}$  IOH-NPs (FMN: flavin mononucleotide) with: a) Scheme of synthesis; b) Particle size according to SEM; c) Aqueous suspensions at daylight and with blue-light excitation; d) Excitation and emission spectra; e) Optical microscopy imaging in cells, and g) in mice after intradermal injection of nanoparticles (Cy5-NHS intravascular vessel stain), (modified reproduction from ref. [34]).

Already in 2008,<sup>[30,34]</sup>  $[ZrO]^{2+}[(HPO_4)_{1-x}(FMN)_x]^{2-}$ , and in particular  $[ZrO]^{2+}[FMN]^{2-}$ , attracted our attention in regard of several aspects: *i*) Its insolubility in water that supports nucleation and growth of nanoparticles; *ii*) The chemical inertness of zirconium phosphates; *iii*) The good biocompatibility of all components (e.g. lethal intake of  $ZrCl_4 > 1$  g/kg);<sup>[41]</sup> *iv*) The replaceability of  $[HPO_4]^{2-}$  and  $[FMN]^{2-}$  in variable ratios.

Due to the low solubility of  $[ZrO]^{2+}[(HPO_4)_{1-x}(FMN)_x]^{2-}$  in water, straightforward aqueous synthesis is possible, avoiding expensive precursors, multistep procedures, and complex structures. Specifically, the synthesis of  $[ZrO]^{2+}[(HPO_4)_{1-x}(FMN)_x]^{2-}$  IOH-NPs comprises the injection of an aqueous solution of  $ZrOCl_2 \cdot 8H_2O$  to an aqueous solution of  $Na_2(FMN)$  and  $Na_2(HPO_4)$  (Figure 2a).<sup>[34]</sup> For controlling particle nucleation and particle growth and for obtaining uniform nanoparticles and colloidal stable suspensions, general aspects of colloid chemistry need to be considered as expressed by the LaMer-Dinegar model.<sup>[42]</sup> Thus, the injection was performed whilst

vigorously stirring at slightly elevated temperatures (55 °C). Moreover, the dye anion was added with 5–10 mol-% excess to guarantee anion-terminated particle surfaces. Subsequent to the synthesis, the IOH-NPs were washed by repeated redispersion and centrifugation in/from water and/or ethanol to remove remaining salts and starting materials. After the purification, the  $[\text{ZrO}]^{2+}[(\text{HPO}_4)_{1-x}(\text{FMN})_x]^{2-}$  IOH-NPs can be easily suspended in polar solvents (e.g., water, ethanol, diethylene glycol) or biological buffers (e.g., HEPES, aqueous dextran). The as-prepared suspensions are colloiddally stable over several months and can contain up to 10 wt-% of the IOH-NPs.<sup>[34]</sup>

Suspensions of  $[\text{ZrO}]^{2+}[(\text{HPO}_4)_{1-x}(\text{FMN})_x]^{2-}$  IOH-NPs are transparent and – depending on their concentration – exhibit a yellow to orange color (Figure 2c). Upon blue-light excitation (LED with  $\lambda_{\text{max}} = 465$  nm), bright green emission (480–650 nm) is observed with its maximum at 530 nm (Figure 2d).<sup>[34]</sup> According to dynamic light scattering (DLS), scanning electron microscopy (SEM), and transmission electron microscopy (TEM), the as-prepared  $[\text{ZrO}]^{2+}[(\text{HPO}_4)_{1-x}(\text{FMN})_x]^{2-}$  IOH-NPs have a mean hydrodynamic diameter of  $39(\pm 12)$  nm and a primary particle diameter of 25–40 nm, respectively (Figure 2b).<sup>[34]</sup> The size distribution indicates that all particles are below 100 nm. In this regard it needs to be taken into account that the synthesis was performed in water without any specific surface agent for controlling nucleation and growth. The determination of the chemical composition of the IOH-NPs is generally challenging, and hence, described in detail in a separate chapter (see 2.4).

The fluorescence of  $[\text{ZrO}]^{2+}[(\text{HPO}_4)_{1-x}(\text{FMN})_x]^{2-}$  – as expected – originates from the FMN anion. Quantum size effects are naturally not involved. Thus, excitation and emission of the  $[\text{ZrO}]^{2+}[(\text{HPO}_4)_{1-x}(\text{FMN})_x]^{2-}$  IOH-NPs (in suspension) can be directly compared to free FMN in solution (Figure 2d).<sup>[34]</sup> The quantum yield of FMN even in solution is comparably low (about 30%).<sup>[43]</sup> Interestingly, the quantum yield of  $[\text{ZrO}]^{2+}[(\text{HPO}_4)_{1-x}(\text{FMN})_x]^{2-}$  with  $28 \pm 2\%$  is identical when considering the experimental significance. Although the  $[\text{FMN}]^{2-}$  anions – and thus, the fluorescence centers – are in close proximity, no concentration quenching was observed. This finding can be ascribed to the amorphous nature of the IOH-NPs that do not exhibit any periodic packing and long-ranging order. Actually, this random distribution of  $[\text{FMN}]^{2-}$  guarantees intense emission. In particular for  $[\text{ZrO}]^{2+}[\text{FMN}]^{2-}$ , the enormous dye load of 81 wt-% and the resulting quasi-infinite reservoir of fluorescent centers per volume of each single nanoparticle leads to intense spotlight-type emission.<sup>[34]</sup> Even certain photobleaching does not noticeably reduce the emission intensity since a great number of fluorescence centers still remains intact (see 2.3: Figure 6c).

Since the IOH-NP concept – including aqueous synthesis, uncomplex material composition and structure, high load of FMN per nanoparticle (81 wt-%) – aims at biomedical application,  $[\text{ZrO}]^{2+}[(\text{HPO}_4)_{1-x}(\text{FMN})_x]^{2-}$ , and especially  $[\text{ZrO}]^{2+}[\text{FMN}]^{2-}$ , were evaluated in *in vitro* and *in vivo* studies regarding fluorescence and imaging performance. Indeed,  $[\text{ZrO}]^{2+}[\text{FMN}]^{2-}$  IOH-NPs show massive uptake into cells. They exhibit high biocompatibility and show intense green emission (Fig-

ure 2f,g).<sup>[34]</sup> In cells or mice the green fluorescence is typically stable over several hours and disappears after 2–3 days with complete dissolution of the IOH-NPs. Toxic or allergic effects – even after a period of two months – were not observed.<sup>[34]</sup> According to TEM and electron-energy loss spectroscopy (EELS), the  $[\text{ZrO}]^{2+}[\text{FMN}]^{2-}$  IOH-NPs localize exclusively in vesicles (Figure 2e). They do not colocalize with mitochondria or nuclei. Thus,  $[\text{ZrO}]^{2+}[\text{FMN}]^{2-}$  IOH-NPs appear to be a suitable tool for staining viable structures.

In spite of the discussed advantages of the  $[\text{ZrO}]^{2+}[(\text{HPO}_4)_{1-x}(\text{FMN})_x]^{2-}$  IOH-NPs, FMN-related green emission is less favorable for biomedical application. On the one hand, cells and tissue show green autofluorescence themselves so that a considerable background is present in addition to the green emission of the IOH-NPs. Moreover, green emission and – even more important – blue light, required for excitation, exhibit low tissue penetration.<sup>[9b,44]</sup> Biomedical issues and optical imaging-based applications in animal models and in humans, therefore, require long-wavelength emission rather in the far-red and near-infrared range, since the light absorption by water and hemoglobin is minimal in this spectral range, resulting in optimal tissue penetration. Taking the composition  $[\text{ZrO}]^{2+}[\text{R}_{\text{Dye}}\text{OPO}_3]^{2-}$  and the concept of the IOH-NPs as a general strategy, phosphate-functionalized fluorescent organic dyes with other luminescence properties as FMN are needed.

Indeed, the IOH-NP concept allows using further fluorescent organic anions and creating a platform of materials. Here, we show the expansion of the concept to  $[\text{ZrO}]^{2+}[\text{PUP}]^{2-}$ ,  $[\text{ZrO}]^{2+}[\text{MFP}]^{2-}$ ,  $[\text{ZrO}]^{2+}[\text{RRP}]^{2-}$ , and  $[\text{ZrO}]^{2+}[\text{DUT}]^{2-}$  with PUP: phenylumbelliferon phosphate, MFP: methylfluorescein phosphate, RRP: resorufin phosphate, and DUT: DY-647 uridine triphosphate (Figure 3a).<sup>[35,36]</sup> All these additional phosphate-based IOH-NPs

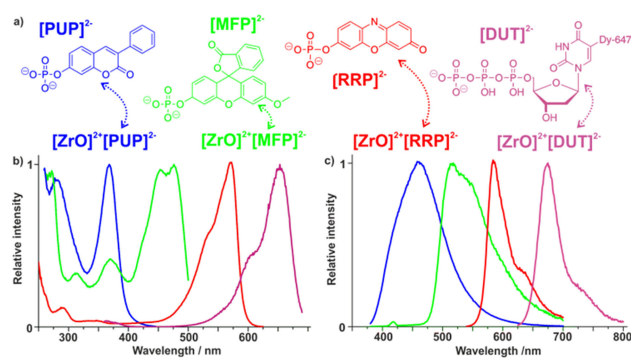


**Figure 3.**  $[\text{ZrO}]^{2+}[\text{PUP}]^{2-}$ ,  $[\text{ZrO}]^{2+}[\text{MFP}]^{2-}$ ,  $[\text{ZrO}]^{2+}[\text{RRP}]^{2-}$ , and  $[\text{ZrO}]^{2+}[\text{DUT}]^{2-}$  IOH-NPs with: a) Structure of fluorescent dye anions; b) Excitation and c) emission spectra (modified reproduction from ref. [35]).

are insoluble in water, too, and can be prepared via aqueous synthesis. They exhibit mean particle diameters of 20–40 nm at high colloidal stability (Figure 4a).  $[\text{ZrO}]^{2+}[\text{PUP}]^{2-}$ ,  $[\text{ZrO}]^{2+}[\text{MFP}]^{2-}$ ,  $[\text{ZrO}]^{2+}[\text{RRP}]^{2-}$ , and  $[\text{ZrO}]^{2+}[\text{DUT}]^{2-}$  show full color emission in the blue (380–600 nm,  $\lambda_{\text{max}} = 458$  nm), green (460–700 nm,  $\lambda_{\text{max}} = 518$  nm), red (550–700 nm,  $\lambda_{\text{max}} = 584$  nm) and near-infrared (630–780 nm,  $\lambda_{\text{max}} = 675$  nm) spectral regime (Fig-

ure 3b,c).<sup>[35]</sup> Due to the quasi-infinite number of fluorescence centers (dye content up to 85 wt-%), all these phosphate-based IOH-NPs again show intense spotlight emission in aqueous suspensions.

To illustrate the biomedical performance,  $[\text{ZrO}]^{2+}[\text{MFP}]^{2-}$ ,  $[\text{ZrO}]^{2+}[\text{RRP}]^{2-}$  and  $[\text{ZrO}]^{2+}[\text{DUT}]^{2-}$  were incubated *in vitro* with murine alveolar macrophages (MHS) cell lines (50  $\mu\text{g}$  IOH-NPs per mL of cell culture medium) to analyze uptake and fluorescence. After incubation (5 h at 37 °C), the internalization of the IOH-NPs is clearly demonstrated and becomes even more evident after 24 h (Figure 4b).<sup>[35]</sup> The granularly structured fluorescence in the macrophages indicates the presence of the IOH-NPs, which was also confirmed by EELS, showing a similar granular structure for the localization of zirconium in the macrophages. Controls with macrophages incubated with the IOH-NPs at 4 °C at reduced metabolic activity as well as macrophages cultivated without IOH-NPs do not show any comparable fluorescence. Furthermore, no relevant toxic effects of  $[\text{ZrO}]^{2+}[\text{MFP}]^{2-}$ ,  $[\text{ZrO}]^{2+}[\text{RRP}]^{2-}$  and  $[\text{ZrO}]^{2+}[\text{DUT}]^{2-}$  were observed with concentrations up to 250  $\mu\text{M}$ .<sup>[35]</sup> After subcutaneous injection in nude mice, the emission is also clearly visible *in vivo* (Figure 4c). Thus, the capability of phosphate-based IOH-NPs for *in vitro* optical imaging is confirmed as a proof-of-the-concept.

### 2.3. Sulfonate-based IOH-NPs

Although phosphate-based IOH-NPs  $[\text{ZrO}]^{2+}[\text{R}_{\text{Dye}}\text{OPO}_3]^{2-}$  already stand for a broad platform of materials with different fluorescent organic anions  $[\text{R}_{\text{Dye}}\text{OPO}_3]^{2-}$ , the number of commercially available fluorescent organic dyes containing a phosphate functionality is limited. Moreover, phosphate-functionalized dyes, and in particular those showing red and infrared emission, are often extremely expensive (up to 500 € per 1 mg).<sup>[45]</sup> In contrast, almost all conventional fluorescent organic dyes are commercially available with sulfonate functions. Functionalization of aromatic organic molecules by sulfonate groups is synthetically straightforward and often used to make such dyes soluble in water.<sup>[21]</sup> As a consequence, almost all organic dye systems – such as coumarins, rhodamines, oxazines, cyanines, etc. – are available with one or more sulfonate group. Introducing such sulfonate-based fluorescent anions  $[\text{R}_{\text{Dye}}(\text{SO}_3)_n]^{n-}$  into the IOH-NP concept could, of course, dramatically broaden the platform of fluorescent nano-materials.

In contrast to phosphate-based fluorescent anions  $[\text{R}_{\text{Dye}}\text{OPO}_3]^{2-}$ , however, sulfonate-based fluorescent anions  $[\text{R}_{\text{Dye}}(\text{SO}_3)_n]^{n-}$  do not form any insoluble compound upon addition of  $[\text{ZrO}]^{2+}$  in water. Taking binary metal sulfates as most suitable reference systems,  $\text{BaSO}_4$  and  $\text{PbSO}_4$  are actually known as the most insoluble sulfates in water.<sup>[32]</sup> Both cations  $\text{Ba}^{2+}$  and  $\text{Pb}^{2+}$ , however, are also known as severely harmful to animate beings.<sup>[46]</sup> Anyway, both cations are not suitable though they also do not form insoluble compounds with sulfonate-based fluorescent anions  $[\text{R}_{\text{Dye}}(\text{SO}_3)_n]^{n-}$ . This can be rationalized based on the monovalent charge of the sulfonate

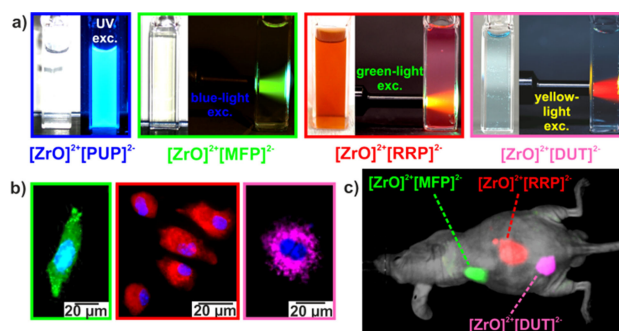


**Figure 4.**  $[\text{ZrO}]^{2+}[\text{PUP}]^{2-}$ ,  $[\text{ZrO}]^{2+}[\text{MFP}]^{2-}$ ,  $[\text{ZrO}]^{2+}[\text{RRP}]^{2-}$ , and  $[\text{ZrO}]^{2+}[\text{DUT}]^{2-}$  IOH-NPs with: a) Aqueous suspensions at daylight and with excitation; b) Emission after uptake by MHS macrophages; c) Emission after subcutaneous injection in nude mouse (modified reproduction from ref. [35]).

group in comparison to the divalent sulfate ion, which reduces the Coulomb interaction significantly. Since the charge of a sulfonate group is fixed, the only option is to choose a cation having a comparable radius as  $\text{Ba}^{2+}/\text{Pb}^{2+}$  (149/133 pm)<sup>[47]</sup> but a higher charge. In this regard,  $\text{La}^{3+}$  (117 pm)<sup>[47]</sup> is promising and indeed results in the formation of insoluble compounds together with sulfonate-based fluorescent anions  $[\text{R}_{\text{Dye}}(\text{SO}_3)_n]^{n-}$ .<sup>[48]</sup> Due to the similarity of the lanthanides, in principle, this holds for all rare-earth-metal ions  $\text{Ln}^{3+}$  ( $\text{Ln}^{3+}$ :  $\text{La}^{3+}$  to  $\text{Lu}^{3+}$ ). From all these ions,  $\text{La}^{3+}$  is interesting due to its low cost. Aiming at novel contrast agents, however,  $\text{Gd}^{3+}$  is even more interesting as it opens the option of multimodal imaging via the fluorescence of the dye anion and the paramagnetism of  $\text{Gd}^{3+}$ .<sup>[6]</sup>

Sulfonate-based IOH-NPs with a general composition  $\text{M}^{3+}_{n/3}[\text{R}_{\text{Dye}}(\text{SO}_3)_n]^{n-}$ ,  $[\text{M}(\text{OH})]^{2+}_{n/2}[\text{R}_{\text{Dye}}(\text{SO}_3)_n]^{n-}$ , or  $[\text{MO}]^+[\text{R}_{\text{Dye}}(\text{SO}_3)_n]^{n-}$  with M: rare-earth metal, and most preferentially with  $\text{La}^{3+}$  or  $\text{Gd}^{3+}$ , can indeed contain a great number of different sulfonate-based dye anions.<sup>[36,48]</sup> As an illustrative example, we take  $\text{M}^{3+}[\text{AMA}]^{3-}$  ( $\text{M} = \text{La}, \text{Gd}$ ) with amaranth red (AMA) as the sulfonate-based fluorescent dye anion (Figure 5a),<sup>[36]</sup> which is also known as E123, C.I. 16185, Acid Red 27, C-Red 46, Ectrot D, or Food

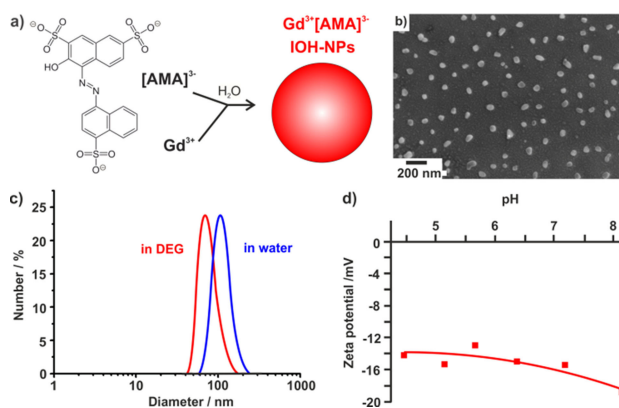


**Figure 5.**  $\text{Gd}^{3+}[\text{AMA}]^{3-}$  IOH-NPs (AMA: amaranth red) with: a) Scheme of synthesis; b) Particle size according to SEM; c) Particle size according to DLS in DEG and in water; d) Zeta potential in water (modified reproduction from ref. [48]).

Red 9.<sup>[49]</sup> AMA is widely used, for instance, in food industry, and can be considered as a less harmful fluorescent dye in comparison to many azo-dyes.

The synthesis of  $M^{3+}[AMA]^{3-}$  ( $M = La, Gd$ ) is comparable to the synthesis of the phosphate-based IOH-NPs and performed by injecting an aqueous solution of  $LaCl_3 \cdot 7H_2O$  or  $GdCl_3 \cdot 6H_2O$  to an aqueous solution of  $Na_3(AMA)$ . Again, general aspects of colloid chemistry according to LaMer's model<sup>[42]</sup> need to be considered to control particle nucleation and particle growth and to obtain nanoparticles and colloidal stable suspensions (Figure 5c). Hence, injection was again performed whilst vigorously stirring at slightly elevated temperature (55 °C). Moreover, the dye anion was used with 10 mol-% excess in relation to the cation to guarantee anion-terminated particle surfaces. After synthesis and purification,  $M^{3+}[AMA]^{3-}$  IOH-NPs can be easily suspended in solvents, such as water, ethanol, diethylene glycol, or biological buffers like HEPES or aqueous dextran. According to the chemical composition,  $La^{3+}[AMA]^{3-}$  and  $Gd^{3+}[AMA]^{3-}$  contain extraordinarily high dye loads of 79 wt-% and 77 wt-%  $[AMA]^{3-}$ , respectively.<sup>[48]</sup>

The particle diameter of the as-prepared  $M^{3+}[AMA]^{3-}$  IOH-NPs was at first measured in DEG, which is known for excellent stabilization of nanoparticles via surface coordination.<sup>[50]</sup> Here, a mean hydrodynamic diameter of  $68 \pm 10$  nm with narrow size distribution was observed (Figure 5c). In water, nanoparticles generally show larger hydrodynamic radii due to a rigid layer of adsorbed solvent molecules. Based on the high polarity and extensive hydrogen bonding networks, this rigid solvent layer is largely expanded in water.<sup>[51]</sup> Thus, a mean hydrodynamic diameter of  $105 \pm 30$  nm was obtained (Figure 5c). Finally, overview SEM images show uniform spherical particles with a mean diameter of  $47 \pm 10$  nm, which was calculated by statistical evaluation of 130 nanoparticles (Figure 5b). Zeta potential analysis of  $La^{3+}[AMA]^{3-}$  and  $Gd^{3+}[AMA]^{3-}$  show negative charging at  $-12.5$  mV in the biologically most relevant pH range of pH 4 to 8 (Figure 5d).<sup>[48]</sup> The resulting electrostatic stabilization is beneficial for both controlling the particle size as well as suppressing agglomeration.

Suspensions of  $La^{3+}[AMA]^{3-}$  and  $Gd^{3+}[AMA]^{3-}$  exhibit a brilliant red color (Figure 6a) and an intense red emission upon excitation by green light (glass fiber with green filter,  $\lambda_{max} = 555$  nm) (Figure 6a).<sup>[48]</sup> Fluorescence spectroscopy indicates strong absorption at 400 to 650 nm and emission at 650 to 800 nm peaking at  $\lambda_{max} = 700$  nm (Figure 6b). Such luminescence features are ideal for biomedical application in terms of low background from autofluorescence and deep penetration of tissue.<sup>[44]</sup>

$M^{3+}[AMA]^{3-}$  IOH-NPs show higher photostability than dissolved AMA ( $Na_3(AMA)$ ) in solution at identical concentration (33 mmol/mL AMA). UV-irradiation of  $M^{3+}[AMA]^{3-}$  suspensions and of dissolved AMA ( $\lambda_{exc} = 310$  nm, 15 h) displays continuous photobleaching with only 27% of pristine emission intensity remaining for dissolved AMA (Figure 6c). In contrast,  $M^{3+}[AMA]^{3-}$  suspensions show almost constant emission intensity over the complete period of irradiation.<sup>[48]</sup> The photostability of the IOH-NPs is even more remarkable when compared to conventional nanoparticle systems with fluorescent organic

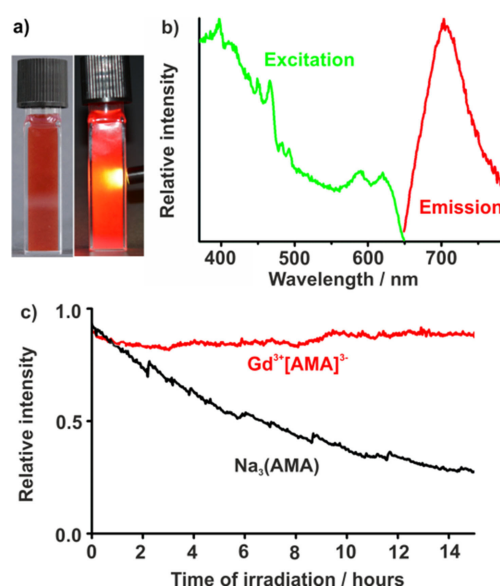


**Figure 6.**  $Gd^{3+}[AMA]^{3-}$  IOH-NPs with: a) Aqueous suspension at daylight and with green light excitation (glass fiber with green filter,  $\lambda_{max} = 555$  nm); b) Excitation and emission spectra; c) Photostability of  $Gd^{3+}[AMA]^{3-}$  (suspension) in comparison to free AMA (solution of  $Na_3(AMA)$ ), all in water, 33 mmol/mL AMA,  $\lambda_{exc} = 310$  nm for 15 h, (modified reproduction from ref. [48]).

dyes encapsulated in inorganic or polymeric matrices (Table 1). They all show considerable photobleaching even on short timescales. The high photostability of the  $M^{3+}[AMA]^{3-}$  IOH-NPs can be attributed, on the one hand, to the extremely high dye load so that certain photobleaching at the particle surface leaves the emission intensity more-or-less unaffected. Despite of strong absorption in the visible (450–700 nm), on the other hand, the IOH-NPs exhibit a high reflectivity in the UV spectral regime ( $< 450$  nm).<sup>[48]</sup> In particular, the absorption of high-energy light is lower, resulting in a reduced formation of reactive oxygen species (ROS), and therefore, a higher photostability.  $SiO_2$  or  $Ca_3(PO_4)_2$ , as widely applied inorganic matrices to encapsulate fluorescent organic dyes, are much less UV-reflective, resulting in a significant photobleaching at daylight (Table 1).

Besides the AMA-based fluorescence,  $Gd^{3+}$ -related paramagnetism of seven unpaired electrons is expected for  $Gd^{3+}[AMA]^{3-}$ . Indeed, powder samples of the IOH-NPs can be already attracted by a bar magnet (Figure 7a). Magnetic measurements quantify the magnetic properties of the as-prepared  $Gd^{3+}[AMA]^{3-}$  to an effective magnetic moment of  $\mu_{eff} = 6.83(1) \mu_B$  per Gd atom and a Weiss constant of  $\theta_p = 4.3(5)$  K (Figure 7b).<sup>[48]</sup> These data are comparable to  $Gd^{3+}$ -based MRI contrast agents, such as the coordination complexes Gd-DPTA (DPTA: diethylenetriaminepentaacetate) and Gd-DOTA (DOTA: 1,4,7,10-tetraazacyclododecane-N,N',N'',N'''-tetraacetic acid),<sup>[55]</sup> which are clinically applied with about 0.1 mmol  $Gd^{3+}$  per kg of body weight.<sup>[56]</sup> An equal  $Gd^{3+}$  content would require about 70 mg of  $Gd^{3+}[AMA]^{3-}$  per kg of body weight. In comparison to standard Gd-DPTA and Gd-DOTA, it must be noted that  $Gd^{3+}$

Encapsulated fluorescent dye	Matrix material	Time of UV irradiation	Intensity after irradiation	Half-lifetime of emission	Ref.
Cy3	Ca <sub>3</sub> (PO <sub>4</sub> ) <sub>2</sub>	300 s	97%	Not measured	[24f] [52]
Cy3	SiO <sub>2</sub>	7 h	98%	Not measured	
Cy5	SiO <sub>2</sub>	200 s	25%	60 s	[24g]
Tetramethyl-rhodamine isothio-cyanate/TRITC	SiO <sub>2</sub>	30 min	88%	Not measured	[53]
Fluorescein iso-thiocyanate/FITC	SiO <sub>2</sub>	30 min	70%	Not measured	[24d]
Indocyanine green/ICG	Ca <sub>3</sub> (PO <sub>4</sub> ) <sub>2</sub>	633 s	50%	633 s	[24h]
Indocyanine green/ICG	PLGA <sup>[a]</sup>	60 min	52%	60 min	[26b] [54]
Nile red	PVK <sup>[a]</sup>	55 min	87%	Not measured	
M <sup>3+</sup> [AMA] <sup>3-</sup>	Hybrid	15 h	100%	Infinite <sup>[b]</sup>	[48]
(M: La, Gd)	(no matrix)				

[a] PLGA: poly(lactic-co-glycolic acid); PVK: poly-N-vinylcarbazole. [b] As no photobleaching and decrease of intensity was observed for M<sup>3+</sup>[AMA]<sup>3-</sup> IOH-NPs on a timescale of 15 h, the formal half-lifetime of emission is infinite.

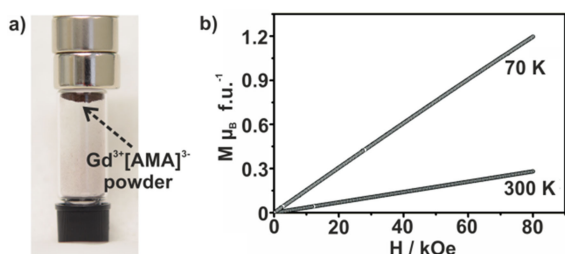


**Figure 7.** Magnetic properties of Gd<sup>3+</sup>[AMA]<sup>3-</sup> IOH-NPs: a) Powder sample upside down with a bar magnet attracting the nanoparticles; b) Magnetization at 70 K and 300 K in dependence of the external magnetic field (modified reproduction from ref. [48]).

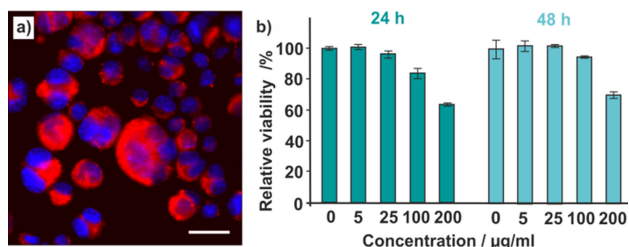


**Figure 8.** Gd<sup>3+</sup>[AMA]<sup>3-</sup> IOH-NPs incubated with MHS macrophages: a) Fluorescence microscopy showing incubated Gd<sup>3+</sup>[AMA]<sup>3-</sup> (24 h after incubation with 50 µg/mL); b) Viability of MHS cells 24 h and 48 h after incubation with different concentrations of the IOH-NPs (scale bar: 20 µm), (modified reproduction from ref. [48]).

[AMA]<sup>3-</sup> IOH-NPs also show fluorescence so that they become suitable for multimodal imaging (OI, MRI).

To further evaluate the applicability of Gd<sup>3+</sup>[AMA]<sup>3-</sup> as a contrast agent, the IOH-NPs were incubated with MHS macrophages.<sup>[57]</sup> Similar to [ZrO]<sup>2+</sup>[FMN]<sup>2-</sup>, a massive uptake of the IOH-NPs was demonstrated by fluorescence microscopy after 5 h of incubation at 37 °C (Figure 8a), whereas internalization is strongly reduced at 4 °C. The viability of the macrophages is unaffected by the uptake of the Gd<sup>3+</sup>[AMA]<sup>3-</sup> IOH-NPs (Figure 8b). Only at high concentrations (≥ 200 µg/mL), the cell viability is decreasing, which, in fact, can be related to a reduced concentration of culture medium. This finding points to a good biocompatibility of the Gd<sup>3+</sup>[AMA]<sup>3-</sup> IOH-NPs.<sup>[48]</sup>

As discussed for phosphate-based IOH-NPs [ZrO]<sup>2+</sup>[R<sub>Dye</sub>OPO<sub>3</sub>]<sup>2-</sup>, M<sup>3+</sup>[AMA]<sup>3-</sup> (M = La, Gd) can be also considered as first representative of a wider platform of sulfonate-based IOH-NPs with a general composition [M]<sup>3+</sup><sub>n/3</sub>[R<sub>Dye</sub>(SO<sub>3</sub>)<sub>n</sub>]<sup>n-</sup>, [M(OH)]<sup>2+</sup><sub>n/2</sub>[R<sub>Dye</sub>(SO<sub>3</sub>)<sub>n</sub>]<sup>n-</sup>, or [MO]<sup>+</sup><sub>n</sub>[R<sub>Dye</sub>(SO<sub>3</sub>)<sub>n</sub>]<sup>n-</sup>.<sup>[58]</sup> Additional examples are, for instance, [Gd(OH)]<sup>2+</sup><sub>2</sub>[CSB]<sup>4-</sup>, [Gd(OH)]<sup>2+</sup><sub>2</sub>[DB71]<sup>4-</sup>, [Gd(OH)]<sup>2+</sup><sub>2</sub>[NFR]<sup>2-</sup>, [Gd(OH)]<sup>2+</sup><sub>2</sub>[AR97]<sup>2-</sup>, and [Gd(OH)]<sup>2+</sup><sub>2</sub>[EB]<sup>4-</sup> containing the sulfonate-based fluorescent anions Chicago Sky Blue ([CSB]<sup>4-</sup>), Direct Blue 71 ([DB71]<sup>4-</sup>), Nuclear Fast Red ([NFR]<sup>2-</sup>), Acid Red 97 ([AR97]<sup>2-</sup>), or Evans Blue ([EB]<sup>4-</sup>) (Figure 9a). All these fluorescent dyes are commercially available and used in solution for staining in cell biology and histology.<sup>[3,9,10]</sup> In particular, this holds for Chicago Sky Blue,<sup>[59]</sup>

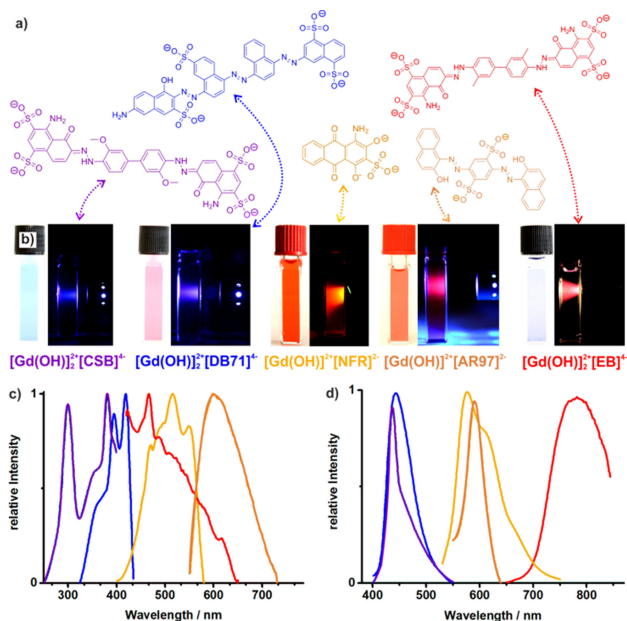


**Figure 9.** [Gd(OH)]<sup>2+</sup><sub>2</sub>[CSB]<sup>4-</sup>, [Gd(OH)]<sup>2+</sup><sub>2</sub>[DB71]<sup>4-</sup>, [Gd(OH)]<sup>2+</sup><sub>2</sub>[NFR]<sup>2-</sup>, [Gd(OH)]<sup>2+</sup><sub>2</sub>[AR97]<sup>2-</sup>, and [Gd(OH)]<sup>2+</sup><sub>2</sub>[EB]<sup>4-</sup> IOH-NPs with: a) Structure of fluorescent dye anions; b) Aqueous suspensions at daylight and with excitation ([Gd(OH)]<sup>2+</sup><sub>2</sub>[CSB]<sup>4-</sup>, [Gd(OH)]<sup>2+</sup><sub>2</sub>[DB71]<sup>4-</sup>, [Gd(OH)]<sup>2+</sup><sub>2</sub>[AR97]<sup>2-</sup> excited via UV-LED; [Gd(OH)]<sup>2+</sup><sub>2</sub>[NFR]<sup>2-</sup> excited via halogen lamp with green glass filter; [Gd(OH)]<sup>2+</sup><sub>2</sub>[EB]<sup>4-</sup> excited via white light halogen lamp); c) Excitation and d) emission spectra (normalized on maximum intensity for direct comparison), (modified reproduction from ref. [48]).

**Table 2.** Average particle size (obtained from SEM), zeta potential (in water at pH 7.0), and dye load of sulfonate-based IOH-NPs.

IOH-NP composition	Particle size from SEM (nm) <sup>[a]</sup>	Zeta potential (mV)	Dye load (wt-%)
Gd <sup>3+</sup> [AMA] <sup>3-</sup>	47 ± 10	-13	77
[Gd(OH)] <sup>2+</sup> <sub>2</sub> [CSB] <sup>4-</sup>	38 ± 5	-26	74
[Gd(OH)] <sup>2+</sup> <sub>2</sub> [DB71] <sup>4-</sup>	37 ± 7	-42	73
[Gd(OH)] <sup>2+</sup> <sub>2</sub> [NFR] <sup>2-</sup>	44 ± 9	-28	70
[Gd(OH)] <sup>2+</sup> <sub>2</sub> [AR97] <sup>2-</sup>	47 ± 6	-19	79
[Gd(OH)] <sup>2+</sup> <sub>2</sub> [EB] <sup>4-</sup>	42 ± 10	-42	77
[GdO] <sup>+</sup> [ICG] <sup>-[b]</sup>	49 ± 8	-27	81
La <sub>4</sub> <sup>3+</sup> [TPPS <sub>4</sub> ] <sub>3</sub> <sup>4-[c]</sup>	68 ± 8	-34	83
Gd <sub>4</sub> <sup>3+</sup> [AIPCS <sub>4</sub> ] <sub>3</sub> <sup>4-[c]</sup>	47 ± 7	-26	81

[a] Statistical average based on > 100 nanoparticles. [b] See 3.1; [c] See 3.2.

Nuclear Fast Red,<sup>[60]</sup> and Evans Blue.<sup>[61]</sup> Similar to M<sup>3+</sup>[AMA]<sup>3-</sup>, the sulfonate-based fluorescent dye anions can be made insoluble upon addition of rare-earth-metal ions such as La<sup>3+</sup> or Gd<sup>3+</sup> to form IOH-NPs with unprecedentedly high dye loads (Table 2).<sup>[58]</sup>

All these sulfonate-based IOH-NPs have mean particle diameters of 40–50 nm at narrow size distribution (Table 2). Additional stabilizers are not required. Moreover, the sulfonate-based IOH-NPs exhibit intense absorption leading to the blue color of [Gd(OH)]<sup>2+</sup><sub>2</sub>[CSB]<sup>4-</sup> and [Gd(OH)]<sup>2+</sup><sub>2</sub>[EB]<sup>4-</sup> as well as to the orange to red color of [Gd(OH)]<sup>2+</sup><sub>2</sub>[NFR]<sup>2-</sup>, [Gd(OH)]<sup>2+</sup><sub>2</sub>[AR97]<sup>2-</sup> and [Gd(OH)]<sup>2+</sup><sub>2</sub>[DB71]<sup>4-</sup> (Figure 9b).<sup>[58]</sup> The absorptive color of the IOH-NPs is similar to the pure organic dyes and again very intense due to the quasi-infinite number of dye anions in each IOH-NP. Accordingly, the IOH-NPs can be also interesting for staining in cell biology and histology as a promising alternative to molecular dyes in solution.

Sulfonate-based IOH-NPs show intense emission upon excitation with visible light (e.g. blue-light LED). Whereas [Gd(OH)]<sup>2+</sup><sub>2</sub>[CSB]<sup>4-</sup> and [Gd(OH)]<sup>2+</sup><sub>2</sub>[DB71]<sup>4-</sup> exhibits emission in the blue spectral regime (Table 3, Figure 9d), [Gd(OH)]<sup>2+</sup><sub>2</sub>[NFR]<sup>2-</sup> and [Gd(OH)]<sup>2+</sup><sub>2</sub>[AR97]<sup>4-</sup> emit yellow and red light. [Gd(OH)]<sup>2+</sup><sub>2</sub>[EB]<sup>2-</sup> shows deep red to infrared emission (Table 3, Figures 9d).<sup>[58]</sup> Most interestingly, fluorescence was yet only reported for NFR, CSB, and EB in the case of the molecular dyes (in solution),<sup>[62]</sup> whereas an emission of DB71 and AR97 was not reported before. Again, the great number of fluorescent centers per nanoparticle not only guarantees intense light absorption

IOH-NP composition	Excitation range (nm)	Emission range (nm)	Emission λ <sub>max</sub> (nm)
Gd <sup>3+</sup> [AMA] <sup>3-</sup>	400–650	650–800	700
[Gd(OH)] <sup>2+</sup> <sub>2</sub> [CSB] <sup>4-</sup>	240–460	400–550	437
[Gd(OH)] <sup>2+</sup> <sub>2</sub> [DB71] <sup>4-</sup>	320–440	400–550	444
[Gd(OH)] <sup>2+</sup> <sub>2</sub> [NFR] <sup>2-</sup>	400–580	520–740	578
[Gd(OH)] <sup>2+</sup> <sub>2</sub> [AR97] <sup>2-</sup>	550–730	550–640	592
[Gd(OH)] <sup>2+</sup> <sub>2</sub> [EB] <sup>4-</sup>	350–640	700–880	782
[GdO] <sup>+</sup> [ICG] <sup>-[a]</sup>	700–820	780–840	810
La <sub>4</sub> <sup>3+</sup> [TPPS <sub>4</sub> ] <sub>3</sub> <sup>4-[b]</sup>	380–600	540–700	585
Gd <sub>4</sub> <sup>3+</sup> [AIPCS <sub>4</sub> ] <sub>3</sub> <sup>4-[b]</sup>	250–400, 550–720	650–770	686

[a] See 3.1; [b] See 3.2.

but also sufficient emission to be detected by the naked eye or via fluorescence microscopy. All in all, the fluorescent sulfonate-based IOH-NPs can be very interesting for optical imaging in cell biology and histology but also for *in vitro* and *in vivo* studies.<sup>[5d,9,63]</sup> Due to the quasi-infinite number of fluorescence centers per nanoparticle – similar to La<sup>3+</sup>[AMA]<sup>3-</sup> and Gd<sup>3+</sup>[AMA]<sup>3-</sup> – low photobleaching is observed (see 2.3: Figure 6c).

## 2.4. Chemical Composition

Proving the chemical composition of the IOH-NPs is challenging. First of all, it needs to be noticed that all IOH-NPs are non-crystalline. They do not show any specific Bragg peak in X-ray diffraction or electron diffraction experiments.<sup>[34,35,48,58]</sup> Consequently, crystal structures of the compounds are unknown. On the other hand, the absence of periodically ordered arrays is advantageous, if not essential in regard of the fluorescence of the IOH-NPs. In the case of crystalline structures with periodically aligned fluorescent organic anions, severe concentration quenching would have been expected that could eradicate the emission of the IOH-NPs partly or completely.<sup>[13]</sup>

In order to elucidate the chemical composition of the IOH-NPs, different analytical methods need to be involved to gain insights at different levels of priority. Obviously, it is the highest priority to prove the presence of the fluorescent organic anion [R<sub>Dye</sub>OPO<sub>3</sub>]<sup>2-</sup> or [R<sub>Dye</sub>(SO<sub>3</sub>)<sub>n</sub>]<sup>n-</sup>. Besides fluorescence spectroscopy, here, Fourier-transformed infrared (FT-IR) spectroscopy is indicative, as exemplarily shown for Gd<sup>3+</sup>[AMA]<sup>3-</sup> (Figure 10a).<sup>[48]</sup> A comparison with the starting material Na<sub>3</sub>(AMA) as reference shows all characteristic vibrations of AMA, including ν(O–H): 3600–3000 cm<sup>-1</sup>, ν(N=N): 1370 cm<sup>-1</sup>, ν(C–N=

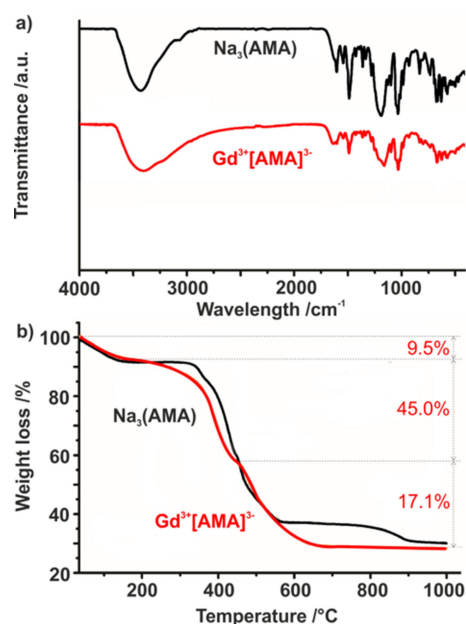
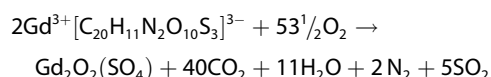


**Figure 10.** Chemical composition of as-prepared Gd<sup>3+</sup>[AMA]<sup>3-</sup> IOH-NPs with: a) FT-IR spectra (Na<sub>3</sub>(AMA) as a reference); b) TG (Na<sub>3</sub>(AMA) as a reference), (modified reproduction from ref. [48]).

N–C): 1230 cm<sup>-1</sup>, ν(SO<sub>3</sub>): 680–420 cm<sup>-1</sup>.<sup>[64]</sup> Certain broadening of the vibrations in the case of the IOH-NPs originates from their non-crystallinity. In addition to the fluorescent dye anion, the presence of the inorganic metal cation is important and qualitatively proven by energy dispersive X-ray spectroscopy (EDXS). Quantification is usually not possible via EDXS since both electron absorption and X-ray emission of the heavy elements (e.g., La, Gd) are too different from the light elements (C, H, N, S, O) for reliable determination.<sup>[48]</sup>

After proving the presence of the inorganic cation and the fluorescent organic anion, their ratio becomes most relevant in order to determine the chemical composition of the IOH-NPs. In this regard, first of all, the charge of the inorganic cation and the fluorescent organic anion should be considered. In addition, the analysis of the total organics content is indicative, especially since inorganic cation and organic anion are of comparable molecular weight. Taking Gd<sup>3+</sup>[AMA]<sup>3-</sup> again as an example, the charges of cation and anion already suggest a cation-to-anion ratio of 1:1, which is validated by performing thermogravimetry (TG) to obtain the total organics content.<sup>[48]</sup> Prior to TG, the as-prepared Gd<sup>3+</sup>[AMA]<sup>3-</sup> IOH-NPs were dried *in vacuo* at room temperature for 8 h to remove all adsorbed volatiles (e.g. water). Thereafter, TG shows a total weight loss of 72% up to a temperature of 1000 °C, which corresponds well to the calculated weight loss of 69% of total organics combustion for the assumed composition Gd<sup>3+</sup>[AMA]<sup>3-</sup> (Figure 10b). Moreover, the thermal remnant of TG analysis was identified via XRD as Gd<sub>2</sub>O<sub>2</sub>(SO<sub>4</sub>). Accordingly, the thermal combustion reaction can be rationalized as follows:<sup>[48]</sup>



In addition to TG analysis, the composition of Gd<sup>3+</sup>[AMA]<sup>3-</sup> can be independently verified by elemental analysis (EA) resulting in C/H/N/S contents of: 32 wt-% C, 3 wt-% H, 4 wt-% N, and 12 wt-% S. Within the experimental error, these data are well in accordance with the calculated values: 36 wt-% C, 2 wt-% H, 4 wt-% N, and 14 wt-% S. Taking all analytical data together (FT-IR, EDX, TG, EA), the chemical composition of Gd<sup>3+</sup>

**Table 4.** Chemical composition of phosphate-based IOH-NPs according to EA (C,H,N,S content), EDX (Zr:P ratio), and TG (total organic combustion).

Compound <sup>[a]</sup>	C content (%-wt, EA) ( <i>calcd</i> )	H content (%-wt, EA) ( <i>calcd</i> )	N content (%-wt, EA) ( <i>calcd</i> )	Zr:P ratio (EDX) ( <i>calcd</i> )	Weight loss (%-wt, TG) ( <i>calcd</i> )
[ZrO] <sup>2+</sup> [RRP] <sup>2-</sup>	26 (34)	3 (2)	3 (4)	1.2:1 (1:1)	43 (48)
[ZrO] <sup>2+</sup> [FMN] <sup>2-</sup>	34 (36)	/	9 (10)	1.0:1 (1:1)	61 (64)
[ZrO] <sup>2+</sup> [MFP] <sup>2-</sup>	42 (47)	4 (3)	0 (0)	1.1:1 (1:1)	62 (64)
[ZrO] <sup>2+</sup> [PUP] <sup>2-</sup>	32 (42)	3 (2)	0 (0)	1.3:1 (1:1)	50 (54)

[a] Note that the composition of [ZrO]<sup>2+</sup>[DUT]<sup>2-</sup> was not studied in detail due to the very high cost of [DUT]<sup>2-</sup> (about 500 € for 1 mg).

**Table 5.** Chemical composition of sulfonate-based IOH-NPs according to EA (C,H,N,S content) and TG (total organic combustion).

Compound	C content (%-wt, EA) ( <i>calcd</i> )	H content (%-wt, EA) ( <i>calcd</i> )	N content (%-wt, EA) ( <i>calcd</i> )	S content (%-wt, EA) ( <i>calcd</i> )	Weight loss (%-wt, TG) ( <i>calcd</i> )
Gd <sup>3+</sup> [AMA] <sup>3-</sup>	32 (36)	3 (2)	4 (4)	12 (14)	72 (69)
[Gd(OH)] <sup>2+</sup> <sub>2</sub> [CSB] <sup>4-</sup>	30 (33)	4 (2)	6 (7)	9 (10)	68 (64)
[Gd(OH)] <sup>2+</sup> <sub>2</sub> [DB71] <sup>4-</sup>	26 (27)	3 (2)	5 (8)	7 (10)	59 (66)
[Gd(OH)] <sup>2+</sup> [NFR] <sup>2-</sup>	35 (33)	3 (2)	3 (3)	8 (6)	62 (56)
[Gd(OH)] <sup>2+</sup> [AR97] <sup>2-</sup>	46 (48)	4 (3)	6 (7)	8 (8)	75 (73)
[Gd(OH)] <sup>2+</sup> <sub>2</sub> [EB] <sup>4-</sup>	31 (33)	4 (2)	6 (7)	9 (11)	67 (64)
[GdO] <sup>+</sup> [ICG] <sup>-[a]</sup>	55 (56)	5 (5)	3 (0)	7 (7)	83 (78)
La <sub>4</sub> <sup>3+</sup> [TPPS] <sub>3</sub> <sup>4-</sup> [b]	46 (47)	3 (2)	5 (5)	10 (11)	76 (76)
Gd <sub>4</sub> <sup>3+</sup> [AIPCS] <sub>3</sub> <sup>4-</sup> [b]	36 (35)	3 (1)	13 (10)	8 (11)	79 (78)

[a] See 3.1; [b] See 3.2.

[AMA]<sup>3-</sup> is reliably substantiated.<sup>[48]</sup> With similar investigations the chemical composition of other phosphate- or sulfonate-based IOH-NPs was determined, as well (Tables 4, 5).

For different reasons the determination of the chemical composition of the IOH-NPs still remains challenging. Thus, the thermal decomposition is complicated in the case of the phosphate-based IOH-NPs due to the encapsulation of the organic content within the metal phosphate formed during thermal decomposition. Actually, such effect is well-known for flame retarding materials. They often contain phosphates to encapsulate organic materials, and thereby, to increase the ignition temperature.<sup>[65]</sup> For analysis of the IOH-NPs, slow heating needs to be performed to guarantee the total combustion of all organic constituents via TG and EA.

For all IOH-NPs, and in particular for sulfonate-based IOH-NPs, oxide atoms and/or hydroxide and water molecules could be coordinated to the metal cation. This is another option to vary the chemical composition of the IOH-NPs as expressed by the formula [M]<sup>3+</sup><sub>n/3</sub>[R<sub>Dye</sub>(SO<sub>3</sub>)<sub>n</sub>]<sup>n-</sup>, [M(OH)]<sup>2+</sup><sub>n/2</sub>[R<sub>Dye</sub>(SO<sub>3</sub>)<sub>n</sub>]<sup>n-</sup>, or [MO]<sup>+</sup><sub>n</sub>[R<sub>Dye</sub>(SO<sub>3</sub>)<sub>n</sub>]<sup>n-</sup>. Due to its low weight (relative to the inorganic cation and the fluorescent dye anion), the coordination of charged species like O<sup>2-</sup> or OH<sup>-</sup> to the metal cation cannot be reliably evidenced based on the above described analytical techniques. On the other hand, the presence of O<sup>2-</sup> or OH<sup>-</sup> would naturally change the net charge of the inorganic cation, and thereby also the ratio of inorganic cation and fluorescent dye anion. This molar ratio, however, can be precisely determined based on TG and EA. Finally, non-charged H<sub>2</sub>O molecules could be coordinated to the inorganic cation. As they do not influence the net charge of the cation or the charge neutrality of the IOH-NPs, and as they only have low weight, such H<sub>2</sub>O coordination (most probably of 1–2 H<sub>2</sub>O molecules per formula unit) cannot be excluded.

Although non-crystalline, finally, the IOH-NPs can be assumed to exhibit layer-type structures. Especially in the case of zirconium phosphates, such as Zr(HPO<sub>4</sub>)<sub>2</sub>·xH<sub>2</sub>O, layered arrangements have been described.<sup>[66]</sup> Layered structures were also often observed for zirconium in combination with organophosphates, and especially, organophosphonates.<sup>[67]</sup> Actually, these compounds are highly relevant as flame retardants.<sup>[68]</sup>

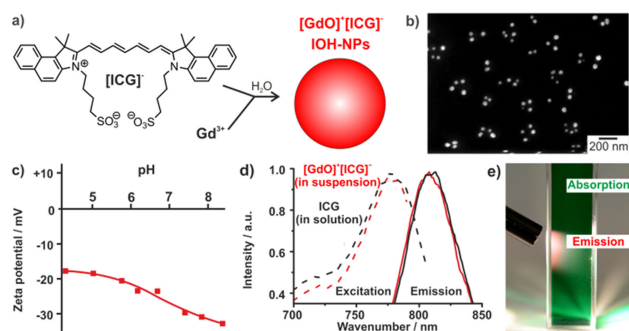


**Figure 11.**  $[\text{GdO}^+][\text{ICG}]^-$  IOH-NPs (ICG: indocyanine green) with: a) Scheme of synthesis; b) Particle size according to SEM; c) Zeta potential in water; d) Excitation and emission spectra (free ICG in solution as reference); e) Aqueous suspension at daylight and excited with white light (modified reproduction from ref. [69]).

Nevertheless, it must be stated that the structural characterization of zirconium phosphates is still lacking, in general.

### 3. Specific Properties of Inorganic-Organic Hybrid Nanoparticles (IOH-NPs)

Subsequent to the illustration of the material concept of the IOH-NPs and after having shown their feasibility for fluorescence detection and optical imaging, we now address more specific functionalities of selected IOH-NPs. This includes  $[\text{GdO}^+][\text{ICG}]^-$  (ICG: indocyanine green) for multimodal imaging,<sup>[69]</sup>  $\text{Gd}_4^{3+}[\text{AIPCS}_4]_3^{4-}$  (AIPCS<sub>4</sub>: aluminium(III) chloride phthalocyanine tetrasulfonate) showing singlet-oxygen generation,<sup>[70]</sup> as well as the dissolution of the IOH-NPs and their use for drug delivery and drug release.

#### 3.1. Multimodal Imaging

To combine the specific assets of different imaging techniques (e.g., resolution, imaging of different types of tissue) and/or to translate preoperative to intraoperative imaging (and *vice versa*), suitable contrast agents for multimodal imaging are highly interesting.<sup>[10]</sup> In this regard, materials with different functionalities were often integrated with high virtuosity into complex nanoarchitectures. This includes, for instance, superparamagnetic iron oxide nanoparticles (SPIONs) and inorganic fluorescent nanoparticles (e.g., Q-dots, lanthanide-doped oxides) or molecular fluorescent dyes (e.g., coumarins, rhodamines, oxazines, cyanines) that were encapsulated in or attached to inorganic or organic matrices (e.g.,  $\text{SiO}_2$ , calcium phosphate, polymers, liposomes, dendrimers).<sup>[3,10]</sup> As discussed before, the complexity of the resulting contrast agents and the sheer number of constituents can be a restriction in itself as all constituents and combinations must be verified individually for clinical approval. In practice, *in vivo* application becomes the more prohibitive the greater the complexity and the more multi-component the employed materials.<sup>[29]</sup> Moreover, the

amount of active contrast agent can be very low in an inert matrix as majority component, which reduces the detection limit.<sup>[24–27]</sup>

In regard to the IOH-NPs, we already discussed optical absorption and fluorescence (see 2.2, 2.3), and we also pointed to  $\text{Gd}^{3+}$  as an optional cation in sulfonate-based IOH-NPs (see 2.3) to implement the IOH-NPs in regard of OI and MRI. Besides imaging, optical absorption, fluorescence, and magnetism can be also used to locate the IOH-NPs in cells and tissue and to determine their *in vitro* and *in vivo* behavior and dissolution. A most interesting type of IOH-NP for multimodal imaging, in this regard, is  $[\text{GdO}^+][\text{ICG}]^-$ , which consists of equimolar amounts of paramagnetic gadolinium as the inorganic cation and  $[\text{ICG}]^-$  as the organic fluorescent dye anion (Figure 11a).<sup>[69]</sup>

Again, an aqueous synthesis was applied to prepare  $[\text{GdO}^+][\text{ICG}]^-$  using  $\text{GdCl}_3 \cdot 6\text{H}_2\text{O}$  and  $\text{Na}[\text{ICG}]$  as the starting materials.  $[\text{GdO}^+][\text{ICG}]^-$  contains 81 wt-%  $[\text{ICG}]^-$  and can be easily suspended in polar solvents (e.g., water, ethanol, diethylene glycol) or biological media (e.g., HEPES, aqueous dextran) with concentrations up to 10 mg/mL. The analytical characterization regarding particle size and chemical composition was performed as described before (see 2.3/2.4: Tables 2, 5). Accordingly, SEM and DLS show mean particle diameters of  $49 \pm 8$  nm and  $50 \pm 9$  nm, respectively, with narrow size distribution (Figure 11b) and a zeta potential of  $-20$  to  $-35$  mV at pH 6–8 (Figure 11c).<sup>[69]</sup>

Aiming at OI, ICG is optimal for biomedical application in many aspects. On the one hand, its strong visible absorption (700–820 nm) and its NIR emission (780–840 nm) are ideal for deep-tissue penetration minimizing the absorbance by water and hemoglobin (Figure 11d).<sup>[9b,44]</sup> Moreover, ICG is well-tolerated (LD<sub>50</sub>: 50–80 mg/kg), approved for clinical use, and already widely used in the clinic for histology.<sup>[71]</sup> Furthermore, ICG is cheap (about 50 € per 1 g)<sup>[72]</sup> in comparison to many alternative commercial red- and infrared-emitting dyes that are conventionally used for OI.<sup>[13,21,45]</sup> On the other hand, ICG as a dissolved molecule has several weaknesses such as: *i*) Rapid binding to human serum albumin and high-density lipoproteins causing agglomeration and rapid clearance via the liver; *ii*) Very short circulation time (half-life of only 2–4 min in mice); *iii*) Low fluorescence quantum yield (only about 5% in water); *iv*) Low chemical stability under physiological conditions due to fast biodegradation; *v*) Rapid photobleaching under light exposure.<sup>[71,73]</sup> Similar to other fluorescent organic dyes, ICG was also often encapsulated in stabilizing matrices (e.g., organic polymers, liposomes, micelles, silica) to overcome these limitations.<sup>[71a,84]</sup> Moreover, ICG has been intercalated in layered double hydroxides (LDHs).<sup>[75]</sup> Again, such inert matrices reduce the available amount of ICG per nanoparticle and lower the intrinsically weak emission intensity even further.

In contrast to ICG solutions, suspensions of  $[\text{GdO}^+][\text{ICG}]^-$  IOH-NPs show intense emission due to the high ICG load (81 wt-%) and the great number of fluorescent centers per nanoparticle (see 2.3: Table 3). Naturally,  $[\text{GdO}^+][\text{ICG}]^-$  (in suspension) exhibits identical fluorescence features as ICG (in solution).<sup>[69]</sup> Accordingly, the dark green aqueous suspensions show deep red emission upon visible light excitation (Fig-

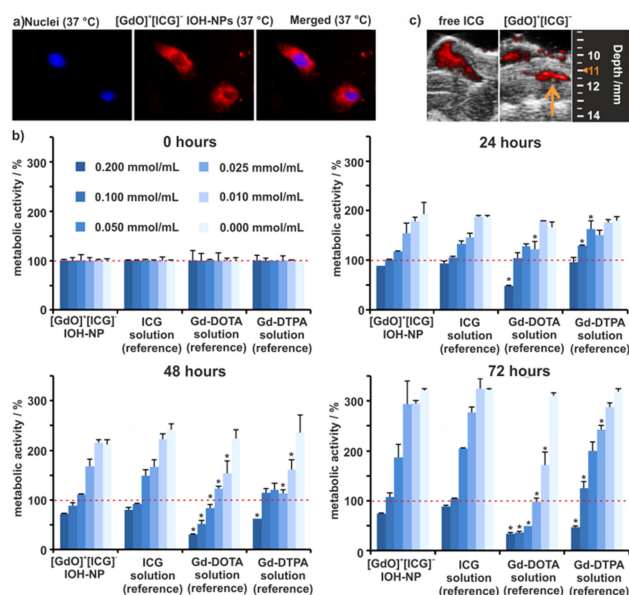


**Figure 12.** *In vitro* studies with  $[\text{GdO}]^+[\text{ICG}]^-$  IOH-NPs: a) Fluorescence images of  $[\text{GdO}]^+[\text{ICG}]^-$  (10  $\mu\text{g}/\text{mL}$  of medium) after 24 h incubation with MHS macrophages at 37 °C; b) Metabolic activity of MHS macrophages after 0, 24, 48 and 72 h cultivation with  $[\text{GdO}]^+[\text{ICG}]^-$  suspensions (dextran-coated); ICG, Gd-DOTA and Gd-DTPA solutions as references (0–0.200 mmol/mL of  $[\text{GdO}]^+[\text{ICG}]^-$ , ICG, Gd-DOTA, Gd-DTPA); c) PAI with  $[\text{GdO}]^+[\text{ICG}]^-$  (suspension) and ICG (solution) at identical concentrations in a dead-mouse phantom (modified reproduction from ref. [69]).

ure 11e). Similar to  $\text{Gd}^{3+}[\text{AMA}]^{3-}$  (see 2.3: Figure 6c),  $[\text{GdO}]^+[\text{ICG}]^-$  IOH-NPs show a higher photostability as well as a greater storage stability and a higher emission intensity as ICG solutions (at identical ICG concentration).<sup>[69]</sup> These features are highly relevant to practical handling since exactly those weaknesses of ICG (in solution) are addressed, which limit its use for fluorescence detection and OI.<sup>[71,73]</sup>

*In vitro* studies with MHS macrophages show an excellent uptake of  $[\text{GdO}]^+[\text{ICG}]^-$  as indicated by their intense emission (Figure 12a). Massive uptake of IOH-NPs was again observed upon incubation at 37 °C, whereas only minimal uptake was observed at 4 °C. This observation indicates an active acquisition of  $[\text{GdO}]^+[\text{ICG}]^-$  by the macrophages. It is to be noticed that the IOH-NPs were coated by dextran to improve the membrane permeability and cell uptake.<sup>[76]</sup> Despite massive internalization of  $[\text{GdO}]^+[\text{ICG}]^-$  IOH-NPs, the metabolic activity and viability of the MHS cells – according to cell proliferation assays – remain almost unaffected (Figure 12b).<sup>[69]</sup> When comparing  $[\text{GdO}]^+[\text{ICG}]^-$  (in suspension) with ICG (in solution) or Gd-DOTA/Gd-DTPA (in solution) as references, the viability of MHS cells treated with the IOH-NPs turned out as only slightly lower as compared to dissolved ICG and significantly higher than for the standard MRI contrast agents Gd-DOTA/Gd-DTPA (Figure 12b).<sup>[69]</sup> Naturally, this comparison was performed at similar concentration of ICG and/or Gd. In regard of its performance as a contrast agent, finally, it must be noted that only  $[\text{GdO}]^+[\text{ICG}]^-$  is multimodal and suitable as contrast agent for OI and MRI.

Whereas free ICG (in solution) is typically not suitable for fluorescence detection due to its low emission,<sup>[71,73]</sup> it is one of

the most promising absorptive contrast agents for PAI.<sup>[9a,77]</sup> Therefore, an evaluation of  $[\text{GdO}]^+[\text{ICG}]^-$  IOH-NPs in regard of its feasibility for PAI seemed obvious. The performance of  $[\text{GdO}]^+[\text{ICG}]^-$  (in suspension) indeed turned out as similar to ICG (in solution) at identical ICG concentration (Figure 12c). Blood vessel phantoms, chicken-breast phantoms, and dead-mouse phantoms showed promising signal intensity and depth of detection, indicating the feasibility of  $[\text{GdO}]^+[\text{ICG}]^-$  IOH-NPs also for PAI.<sup>[69]</sup>

Besides *in vitro* studies, the multimodal features of  $[\text{GdO}]^+[\text{ICG}]^-$  in terms of MRI and OI were evaluated *in vivo*. In response to increasing concentrations, the IOH-NPs clearly result in a reduction of the  $T_1$ -relaxation (Figure 13a).<sup>[69]</sup> The

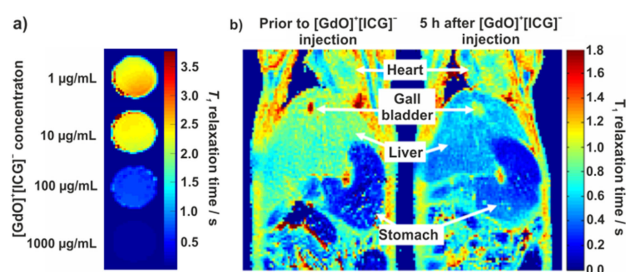


**Figure 13.**  $[\text{GdO}]^+[\text{ICG}]^-$  IOH-NPs (dextran-coated) as MR contrast agent: a) Maps of  $T_1$ -relaxation time calculated for varying concentrations of dextran-coated IOH-NPs; b) Mice imaged before and 5 h after injection with  $[\text{GdO}]^+[\text{ICG}]^-$  IOH-NPs. Images show  $T_1$ -relaxation time heat maps with a noticeably reduced relaxation in the gall bladder and liver (by 35%), (modified reproduction from ref. [69]).

specific relaxivity ( $r_1$ ) per gadolinium at 7 Tesla was determined to  $8.0 \pm 0.4 \text{ mM}^{-1} \text{ s}^{-1}$  for dextran-coated  $[\text{GdO}]^+[\text{ICG}]^-$ . In fact, the relaxivity is even higher than for Gd-DTPA or Gd-DOTA ( $3\text{--}5 \text{ mM}^{-1} \text{ s}^{-1}$ ).<sup>[65,55]</sup> *In vivo*, mice were imaged before and 5 h after intravenous injection of  $[\text{GdO}]^+[\text{ICG}]^-$  IOH-NP suspensions resulting in  $T_1$ -relaxation heat maps with a noticeable decrease in relaxation time in the gall bladder and liver (Figure 13b). Both results indicate that  $[\text{GdO}]^+[\text{ICG}]^-$  IOH-NPs can be a promising MRI contrast agent.

In parallel with MRI, mice were also imaged *in vivo* with fluorescence molecular tomography (FMT) and *post mortem* – after exposing the organs – using fluorescence reflectance imaging (FRI) (Figure 14). Again,  $[\text{GdO}]^+[\text{ICG}]^-$  IOH-NPs can be clearly detected.<sup>[69]</sup> Detection via FMT is even possible over a time range of several hours. In combination, FMT and FRI demonstrate that  $[\text{GdO}]^+[\text{ICG}]^-$  IOH-NPs are suitable as multimodal contrast agents *in vitro* as well as *in vivo* for OI, PAI and MRI. Straightforward synthesis and low material complexity of  $[\text{GdO}]^+[\text{ICG}]^-$  IOH-NPs are additional assets in comparison to many contrast agents discussed in the literature. In the clinics,  $[\text{GdO}]^+[\text{ICG}]^-$  IOH-NPs could allow to combine the presentation of different types of tissue, for instance, soft tissue via MRI, blood vessels via PAI, and single cells via OI.<sup>[3,5,55]</sup>

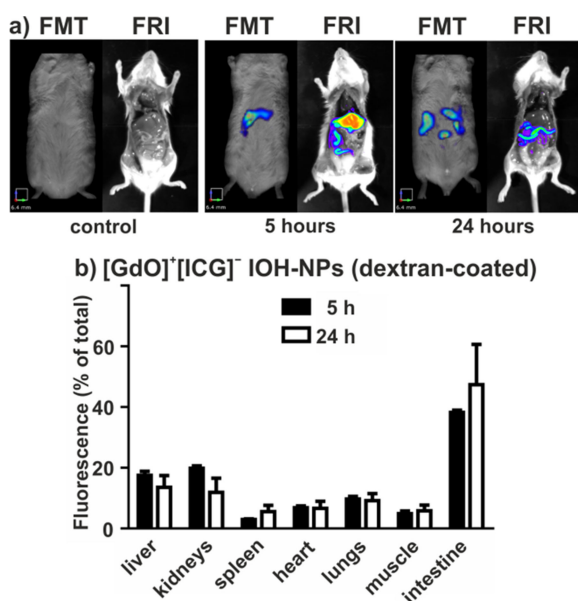


**Figure 14.**  $[\text{GdO}]^{3+}[\text{ICG}]^{-}$  IOH-NPs (dextran-coated) as OI contrast agent: a) *In vivo* and *post mortem* fluorescence images acquired of mice 0, 5 and 24 h after  $[\text{GdO}]^{3+}[\text{ICG}]^{-}$  injection using fluorescence molecular tomography (FMT) and fluorescence reflectance imaging (FRI). Organs were removed and the fluorescence distribution quantified for (b)  $[\text{GdO}]^{3+}[\text{ICG}]^{-}$  (modified reproduction from ref. [69]).

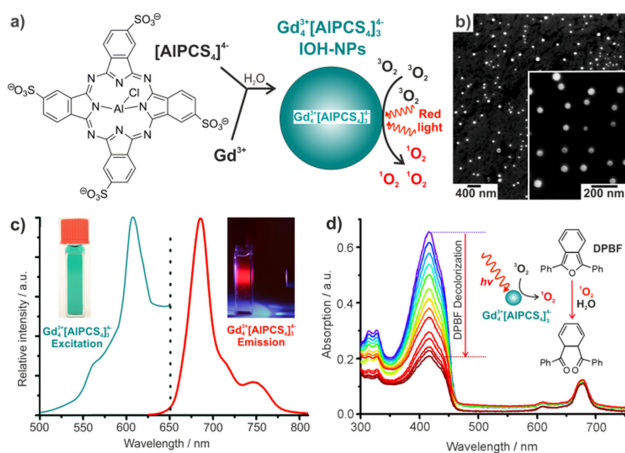


**Figure 15.**  $\text{Gd}_4^{3+}[\text{AIPCS}_4]_3^{4-}$  IOH-NPs (AIPCS<sub>2</sub>: aluminium(III) chloride phthalocyanine tetrasulfonate) with: a) Scheme of synthesis; b) Particle size according to SEM; c) Excitation and emission spectra with aqueous suspensions at daylight and with excitation (blue-light LED); d) Determination of the quantum yield ( $\varphi_{\text{O}_2}$ ) for  $^1\text{O}_2$  production via the DPBF method (modified reproduction from ref. [70]).

### 3.2. Singlet Oxygen Production

In addition to multimodal imaging, specific IOH-NPs are also suitable for photoactivated singlet-oxygen ( $^1\text{O}_2$ ) generation. For this purpose, the sulfonate-based anions aluminium(III) chloride phthalocyanine tetrasulfonate ( $[\text{AIPCS}_4]^{4-}$ , Figure 15a) and tetraphenylporphyrin sulfonate ( $[\text{TPPS}_4]^{4-}$ , not shown) were applied as functional organic anions.<sup>[70,78]</sup> The resulting IOH-NPs have a composition  $\text{Gd}_4^{3+}[\text{AIPCS}_4]_3^{4-}$  and  $\text{La}_4^{3+}[\text{TPPS}_4]_3^{4-}$ . Both contain extremely high photoactivator concentrations with 81 wt-%

$[\text{AIPCS}_4]_3^{4-}$  in  $\text{Gd}_4^{3+}[\text{AIPCS}_4]_3^{4-}$  and 83 wt-%  $[\text{TPPS}_4]_3^{4-}$  in  $\text{La}_4^{3+}[\text{TPPS}_4]_3^{4-}$ . The synthesis was again performed in water using  $\text{GdCl}_3 \times 6\text{H}_2\text{O}$  or  $\text{LaCl}_3 \times 6\text{H}_2\text{O}$  and  $\text{H}_4\text{AIPCS}_4$  or  $\text{H}_4\text{TPPS}_4$  as starting materials and resulted in transparent greenish blue  $\text{Gd}_4^{3+}[\text{AIPCS}_4]_3^{4-}$  and brownish  $\text{La}_4^{3+}[\text{TPPS}_4]_3^{4-}$  suspensions (Figure 15c).  $\text{Gd}_4^{3+}[\text{AIPCS}_4]_3^{4-}$  and  $\text{La}_4^{3+}[\text{TPPS}_4]_3^{4-}$  exhibit mean diameters of 47 and 56 nm, respectively (Figure 15b; see 2.3: Table 2).<sup>[70,78]</sup> Their chemical composition was validated by FT-IR, TG, EDXS and EA (see 2.4: Table 5). Both  $\text{Gd}_4^{3+}[\text{AIPCS}_4]_3^{4-}$  and  $\text{La}_4^{3+}[\text{TPPS}_4]_3^{4-}$  also show visible emission, which, in principle, is also sufficient for fluorescence detection and OI (see 2.3: Table 3).

In fact, phthalocyanines as well as porphyrins are well-known for efficient photoactivated  $^1\text{O}_2$  generation. Both are already discussed for applications such as the selective oxidation in organic synthesis (e.g., cycloadditions, Diels-Alder reactions, Ene reactions, heteroatom oxidations),<sup>[79]</sup> the degradation of organic molecules and germs (e.g. for water purification),<sup>[80]</sup> and photodynamic therapy (PDT) (most often used for tumor therapy).<sup>[81]</sup> Certain porphyrins and phthalocyanines are already approved in the clinics.<sup>[81c,d,82]</sup> Aiming at PDT, molecular photosensitizers in solution, however, have certain disadvantages, such as low solubility in water and rapid aggregation under physiological conditions. Both reduce the efficiency of  $^1\text{O}_2$  production and result in limited membrane permeability and poor cell uptake.<sup>[83]</sup> Again, it was suggested to immobilize the molecular porphyrins and phthalocyanines on/in nanosized/nanoporous substrates, such as silica and gold nanoparticles as well as carbon nanotubes,<sup>[81b,83,84]</sup> which again leads to only low amounts of the active molecular photocatalyst (typically <10 wt-%). Moreover, metalorganic frameworks containing porphyrin linkers were presented.<sup>[85]</sup> For medical application, in particular, encapsulation in vesicles and liposomes or functionalization with hydrophilic capping ligands was established.<sup>[86]</sup> However, these measures also enhance the material complexity, and any encapsulation/capping, as a matter of fact, blocks the active sites of the photocatalysts.

The feasibility of  $\text{Gd}_4^{3+}[\text{AIPCS}_4]_3^{4-}$  and  $\text{La}_4^{3+}[\text{TPPS}_4]_3^{4-}$  for  $^1\text{O}_2$  production was validated by the DPBF method (DPBF: 1,3-diphenylisobenzofuran)<sup>[87]</sup> and the iodide method.<sup>[88]</sup> DPBF is oxidized in the presence of  $^1\text{O}_2$  as indicated by the vanishing characteristic red color of DPBF (Figure 15d). The decreasing absorption at 420 nm can be easily monitored by UV-Vis spectroscopy and results in a quantum yield of 33% for  $^1\text{O}_2$  production of  $\text{Gd}_4^{3+}[\text{AIPCS}_4]_3^{4-}$  IOH-NPs (in suspension). This value matches very well with molecular  $\text{H}_4\text{AIPCS}_4$  (35%, in solution).<sup>[87]</sup> This finding is even more interesting, since  $\text{H}_4\text{AIPCS}_4$  is known for rapid photodegradation in solution. In contrast,  $\text{Gd}_4^{3+}[\text{AIPCS}_4]_3^{4-}$  IOH-NPs show good photostability without any considerable concentration quenching.<sup>[70]</sup> Both can be explained, on the one hand, by the great phthalocyanine/porphyrin reservoir, and, on the other hand, by the non-crystallinity of the IOH-NPs that avoids any ordered alignment of the phthalocyanine anions. The quantum yield of  $^1\text{O}_2$  generation of  $\text{La}_4^{3+}[\text{TPPS}_4]_3^{4-}$  cannot be performed via the more common DPBF method since the absorption of  $[\text{TPPS}_4]_3^{4-}$  overlays the DPBF absorption band. Instead, the iodide method

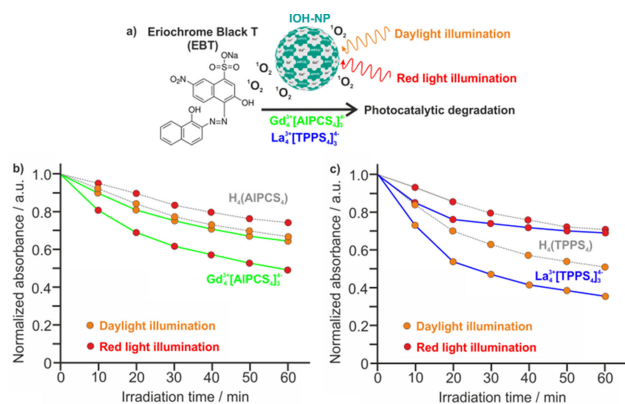


**Figure 16.** Photocatalytic dye degradation of Eriochrome Black T (EBT, monitored at 528 nm,  $c(\text{EBT}) = 0.03 \mu\text{mol/L}$ ) with: a) Scheme of photocatalytic degradation with structure of EBT; b) Comparison of  $\text{Gd}_4^{3+}[\text{AIPCS}_4]_3^{4-}$  (in suspension) with  $\text{H}_4\text{AIPCS}_4$  (in solution); c) Comparison of  $\text{La}_4^{3+}[\text{TPPS}_4]_3^{4-}$  (in suspension) with  $\text{H}_4\text{TPPS}_4$  (in solution). Illumination with simulated daylight (halogen lamp) and red light (halogen lamp with red filter,  $\lambda > 610 \text{ nm}$ ).  $\text{Gd}_4^{3+}[\text{AIPCS}_4]_3^{4-}$ ,  $\text{La}_4^{3+}[\text{TPPS}_4]_3^{4-}$ ,  $\text{H}_4\text{AIPCS}_4$ , and  $\text{H}_4\text{TPPS}_4$ , compared at identical phthalocyanine/porphyrin concentration ( $8 \mu\text{M Gd}_4^{3+}[\text{AIPCS}_4]_3^{4-}/\text{La}_4^{3+}[\text{TPPS}_4]_3^{4-}$ ;  $24 \mu\text{M H}_4\text{AIPCS}_4/\text{H}_4\text{TPPS}_4$ ), (modified reproduction from ref. [70]).

was applied here,<sup>[88]</sup> resulting in a quantum yield of 49% for  $\text{La}_4^{3+}[\text{TPPS}_4]_3^{4-}$  (in suspension), which is again close to the value of molecular  $\text{H}_4\text{TPPS}_4$  (51%, in solution).<sup>[88]</sup>

To determine the photocatalytic performance of  $\text{Gd}_4^{3+}[\text{AIPCS}_4]_3^{4-}$  and  $\text{La}_4^{3+}[\text{TPPS}_4]_3^{4-}$  (Figure 16a), both were first conceptually evaluated in regard of the photocatalytic degradation of Eriochrome Black T (EBT). EBT was chosen as a model dye since its absorption ( $\lambda_{\text{max}} = 525 \text{ nm}$ ) does not overlap that of  $\text{Gd}_4^{3+}[\text{AIPCS}_4]_3^{4-}$  ( $\lambda_{\text{max}} = 670 \text{ nm}$ ) and  $\text{La}_4^{3+}[\text{TPPS}_4]_3^{4-}$  ( $\lambda_{\text{max}} = 425 \text{ nm}$ ). The photocatalytic degradation was studied with simulated daylight (halogen lamp) as well as with red-light illumination (glass filter with  $\lambda > 610 \text{ nm}$ ) by comparing  $\text{Gd}_4^{3+}[\text{AIPCS}_4]_3^{4-}$  and  $\text{La}_4^{3+}[\text{TPPS}_4]_3^{4-}$  (in suspension) with  $\text{H}_4\text{AIPCS}_4$  and  $\text{H}_4\text{TPPS}_4$  (in solution) as references.<sup>[70]</sup> Despite of identical concentrations of the photoactive phthalocyanine/porphyrin, the IOH-NPs (in suspension) show significantly higher photoactivity and faster EBT degradation than the dissolved references (Figure 16b,c). This higher performance can be rationalized when considering the negative charges of all sulfonate-based anions at neutral pH (i.e.,  $[\text{AIPCS}_4]_3^{4-}$ ,  $[\text{TPPS}_4]_3^{4-}$ ,  $[\text{EBT}]^-$ ) leading to a stronger electrostatic repulsion of the dissolved species than to the non-charged IOH-NPs.<sup>[89]</sup> Moreover, the local absorption intensity of the IOH-NPs (in suspension) is higher due to the great number of absorbing centers per volume of each nanoparticle compared to the widely separated  $\text{H}_4\text{AIPCS}_4$  and  $\text{H}_4\text{TPPS}_4$  molecules (in solution).

With the above described features and performance – including the extremely high phthalocyanine/porphyrin load and the promising photocatalytic effect with daylight illumination – the  $\text{Gd}_4^{3+}[\text{AIPCS}_4]_3^{4-}$  and  $\text{La}_4^{3+}[\text{TPPS}_4]_3^{4-}$  IOH-NPs can be highly interesting not only for photocatalytic dye degradation but also for PDT.<sup>[78]</sup> PDT is generally considered as a useful addition to the armory against cancer since it is minimally invasive and non-damaging to healthy tissue. Specifically, PDT

is known for treatment of near-surface tumors (e.g., skin, esophagus or intestinal cancer)<sup>[90]</sup> and intensely discussed for post-surgery treatment to kill cancer cells that may remain after extraction of the solid primary tumor.<sup>[91]</sup> In view of deep-tissue penetration, the long-wavelength excitation of  $\text{Gd}_4^{3+}[\text{AIPCS}_4]_3^{4-}$  (550–720 nm) seems most interesting to PDT and was therefore studied *in vitro* and *in vivo*.  $\text{Gd}_4^{3+}[\text{AIPCS}_4]_3^{4-}$  IOH-NPs are even more interesting since  $\text{H}_4\text{AIPCS}_4$  (in solution) is already approved for PDT.<sup>[92]</sup> Based on the paramagnetism of  $\text{Gd}^{3+}$  and the deep red emission of  $[\text{AIPCS}_4]_3^{4-}$ , furthermore,  $\text{Gd}_4^{3+}[\text{AIPCS}_4]_3^{4-}$  IOH-NPs are also suitable for multimodal imaging including MRI and OI. With these features,  $\text{Gd}_4^{3+}[\text{AIPCS}_4]_3^{4-}$  can be an advantageous addition to existing nanoparticulate photosensitizers for PDT. So far, this includes inorganic nanoparticles such as  $\text{TiO}_2$  or  $\text{ZnO}$  as well as rare-earth based up-converters,<sup>[93]</sup> which suffer from UV-activation (i.e.,  $\text{TiO}_2$ ,  $\text{ZnO}$ ) being harmful to cells<sup>[93a,b]</sup> or narrow-line laser-type excitation (i.e. up-conversion via *f-f* transitions on rare-earth metals).<sup>[93c,d]</sup>

The feasibility of  $\text{Gd}_4^{3+}[\text{AIPCS}_4]_3^{4-}$  IOH-NPs was demonstrated *in vitro* with human liver carcinoma (HepG2) cells and human cervix carcinoma (HeLa) cells.<sup>[78]</sup> The incubation of cells with dextran-coated  $\text{Gd}_4^{3+}[\text{AIPCS}_4]_3^{4-}$  IOH-NPs proves good cellular uptake as indicated by an intense red fluorescence (Figure 17a,b). Moreover, efficient photoactivated  $^1\text{O}_2$  genera-

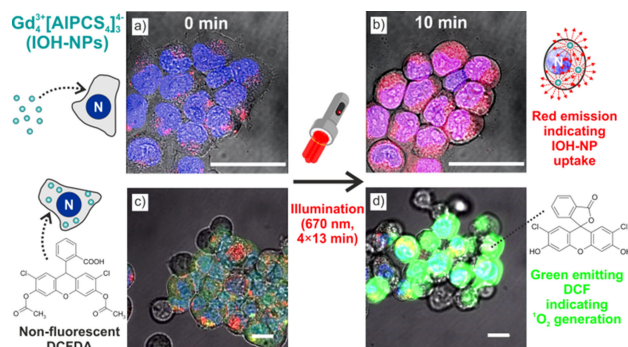


**Figure 17.** *In vitro* evaluation of  $\text{Gd}_4^{3+}[\text{AIPCS}_4]_3^{4-}$  IOH-NPs (20  $\mu\text{M}$ ) in HepG2 cells after 24 h of incubation: a) Prior to illumination in daylight and b) after 10 min of illumination with red fluorescence indicating the IOH-NP uptake (nuclei stained with Hoechst 33342); c) Cells treated with DCFDA prior and d) after illumination with green fluorescence of DCF indicating ROS generation. Illumination performed by scanning slides 4-times for 13 min using scan cycles at 670 nm (Pearl Imager, LI-COR Biosciences; N: nucleus; scale bar: 20  $\mu\text{m}$ ), (modified reproduction from ref. [78]).

tion and ROS production upon illumination ( $\lambda_{\text{exc}} = 635 \text{ nm}$ ) was evidenced with DCFDA-treated (DCFDA: profluorescent 2',7'-dichlorofluorescein diacetate) cells, which show bright green fluorescence due to 7'-dichlorofluorescein (DCF) produced in the presence of ROS (Figure 17c,d). Furthermore, a comparison of the  $\text{Gd}_4^{3+}[\text{AIPCS}_4]_3^{4-}$  IOH-NPs (in suspension) with free  $\text{H}_4\text{AIPCS}_4$  (in solution) at identical phthalocyanine concentration (20  $\mu\text{M}$ ) indicates the  $\text{Gd}_4^{3+}[\text{AIPCS}_4]_3^{4-}$ -treated cells to be much more active in generating photoinduced ROS.<sup>[78]</sup>

The phototoxic effect of the  $\text{Gd}_4^{3+}[\text{AIPCS}_4]_3^{4-}$  IOH-NPs (in suspension) was quantified by MTT toxicity assays and compared to molecular  $\text{H}_4\text{AIPCS}_4$  (in solution) at identical

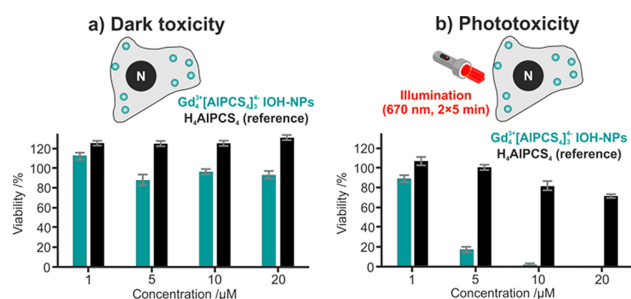


**Figure 18.** *In vitro* phototoxicity of  $Gd_4^{3+}[AIPCS_4]_3^{4-}$  IOH-NPs as indicated by MTT assays: a) Cells treated with  $Gd_4^{3+}[AIPCS_4]_3^{4-}$  IOH-NPs (green bars) and with dissolved  $H_4AIPCS_4$  (black bars) after 72 h of incubation in darkness; b) Cells treated similarly and with illumination at 670 nm for 2 × 5 min (statistical error bars calculated from  $n = 6$ ; significance determined according to student's  $t$ -test with  $p < 0.05$ ; N: nucleus), (reproduction from ref. [78]).

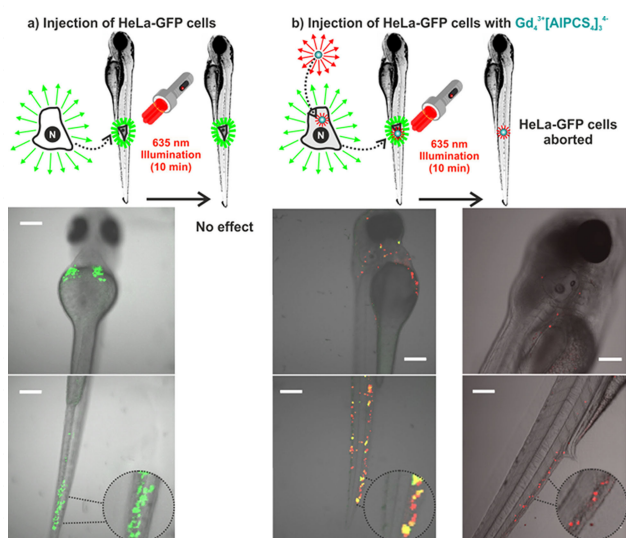


**Figure 19.** *In vivo* phototoxicity and imaging of  $Gd_4^{3+}[AIPCS_4]_3^{4-}$  IOH-NP-treated HeLa-GFP cells in zebrafish larvae after NIR illumination. Larvae were xenografted with GFP expressing and  $Gd_4^{3+}[AIPCS_4]_3^{4-}$  IOH-NPs (5 μM) pretreated HeLa cells. After 24 h, the larvae were illuminated for 10 min at 670 nm and thereafter imaged using fluorescent confocal microscopy: a) GFP expression exited at 488 nm (Argon laser) and the emission detected at 498–540 nm; b)  $Gd_4^{3+}[AIPCS_4]_3^{4-}$  IOH-NPs excited at 635 nm and the emission detected at 644–786 nm. Upon illumination the cells were losing GFP expression and the tumors were reduced in size (N: nucleus; scale bar: 200 μm), (modified reproduction from ref. [78]).

phthalocyanine concentrations (1–20 μM) (Figure 18).<sup>[78]</sup> Metabolically active cells reduce the yellow tetrazolium compound 3-(4,5-dimethylthiazol-2-yl)2,5-diphenyltetrazolium bromide (MTT) to a purple formazan, which can be monitored photometrically. First of all, the dark toxicity was assessed and showed slightly higher toxicity of the IOH-NPs in comparison to  $H_4AIPCS_4$  in solution (Figure 18a). Thereafter, the phototoxicity subsequent to light exposure (2 × 5 min, 670 nm) was determined and results in a significantly higher cytotoxic effect with  $Gd_4^{3+}[AIPCS_4]_3^{4-}$ -treated cells (in suspension,  $LD_{50} < 5 \mu M$ ) compared to cells treated with molecular  $H_4AIPCS_4$  (in solution,  $LD_{50} > 20 \mu M$ ) (Figure 18b). Moreover, a suppressed angiogenesis of microcapillary networks was detected after treatment of

endothelial cells with  $Gd_4^{3+}[AIPCS_4]_3^{4-}$  *in vitro* and subsequent illumination.<sup>[78]</sup> Altogether, these results validate the phototoxic activity and performance of the  $Gd_4^{3+}[AIPCS_4]_3^{4-}$  IOH-NPs and their advantage over dissolved  $H_4AIPCS_4$ .

Finally, the phototoxic effect of the  $Gd_4^{3+}[AIPCS_4]_3^{4-}$  IOH-NPs was evaluated in an *in vivo* zebrafish tumor model. Zebrafishes are generally known as a suitable platform for testing and refining therapies in the preclinical phase of drug development.<sup>[94]</sup> They are easier to handle than mice and allow a direct readout by OI due to their small size and transparency. In our study,  $Gd_4^{3+}[AIPCS_4]_3^{4-}$  IOH-NPs were first incubated with HeLa-GFP cells expressing green fluorescent proteins (GFP). Thereafter, the IOH-NP-pretreated HeLa-GFP cells were injected into the cardinal vein of zebrafish larvae to induce tumors (Figure 19a). The  $Gd_4^{3+}[AIPCS_4]_3^{4-}$  IOH-NP-pretreated HeLa-GFP cells could be easily detected in the zebrafish larvae by their red and green emission (Figure 19b). Upon light exposure over a certain period of time (10 min, 670 nm), the green emission of the HeLa-GFP cells is significantly decreased, which indicates their reduced viability. Finally, only the red emission of the  $Gd_4^{3+}[AIPCS_4]_3^{4-}$  IOH-NPs remains at the position of cellular debris and necrotic tumors (Figure 19b).<sup>[78]</sup> HeLa-GFP cells without  $Gd_4^{3+}[AIPCS_4]_3^{4-}$  IOH-NPs were injected into zebrafish larvae as a control and did not show any effect and vanishing of the green emission at all (Figure 19a). As a result, the phototoxic performance of the  $Gd_4^{3+}[AIPCS_4]_3^{4-}$  IOH-NPs is clearly shown *in vivo*. Specific optimization of parameters – such as the concentration of the IOH-NPs, the duration of illumination, certain repeat treatments – is of course needed to reliably explore the optimal treatment efficiency and to establish therapy protocols.

### 3.3. Dissolution of IOH-NPs

In cell and mouse studies of all IOH-NPs, and in particular of the phosphate-based  $[ZrO]^{2+}[R_{Dye}OPO_3]^{2-}$  IOH-NPs, the fluorescence was observed to vanish on a timescale of several hours to some days.<sup>[34,35]</sup> Typically, no fluorescence and no nanoparticle remains could be identified after 3–4 days. This finding points to a slow dissolution of the IOH-NPs, which can be rationalized upon hydrolysis of the P–O–C phosphorus acid ester bond, resulting in the dissolved species  $[ZrO]^{2+}$ ,  $[HPO_4]^{2-}$  and  $R_{Dye}OH$  (Figure 20). Such dissolution can be triggered by acid or base catalysis as well as by ubiquitous phosphatases in cells and tissue.<sup>[95]</sup> In fact, such dissolution is ideal in terms of biocompatibility and biodegradability, especially if there is no specific toxicity of the dissolved species and if all species are completely released from cells, tissue and body after certain period of time.

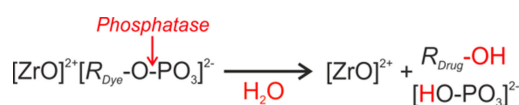


**Figure 20.** Model reaction for the slow metabolic dissolution of  $[ZrO]^{2+}[R_{Dye}OPO_3]^{2-}$  IOH-NPs (modified reproduction from ref. [35]).

Various *in vitro* and *in vivo* studies in the meantime have proven that no specific toxicity or allergic reaction is caused by the IOH-NPs.<sup>[34,35,48,58,69,78]</sup> In particular, this holds for the cations  $[\text{ZrO}]^{2+}$  and  $\text{Gd}^{3+}/[\text{Gd}(\text{OH})_2]^{2+}/[\text{GdO}]^+$ . Even for the latter, a lower toxicity as compared to the standard MRI contrast agents Gd-DOTA and Gd-DTPA was observed.<sup>[48,58,69,78]</sup> A detection of the dissolved species after their release from the IOH-NPs, however, is not straightforward. On the one hand, immediate dilution of the dissolved species in the volume of cells, tissue and body leads to only low concentrations remaining, and thereby hampers the detection. Analyzing  $[\text{HPO}_4]^{2-}$  and  $R_{\text{Dye}}\text{OH}$  is difficult anyway due to the ubiquitous physiological availability of phosphate and the rapid metabolic decomposition of the fluorescent dye anion. Here, radio-labeling could be a useful option. Tracking of  $[\text{ZrO}]^{2+}$  is easier due to its absence in animate beings. *In vivo* studies indeed show that the pristine amount of injected zirconium in  $[\text{ZrO}]^{2+}[\text{R}_{\text{Dye}}\text{OPO}_3]^{2-}$  IOH-NPs can be typically retrieved from urine on a time scale of 2–4 days.

To verify the dissolution of the IOH-NPs, we have initiated several test reactions with suitable model compounds. A first example relates to  $[\text{ZrO}]^{2+}[\text{UFP}]^{2-}$  IOH-NPs (UFP: umbelliferone phosphate).<sup>[96]</sup>  $[\text{ZrO}]^{2+}[\text{UFP}]^{2-}$  exhibits a typical particle size of  $47 \pm 9$  nm and shows characteristic, but weak blue emission ( $\lambda_{\text{max}} = 455$  nm) of UFP upon UV excitation ( $\lambda_{\text{exc}} = 366$  nm). Although less interesting for imaging purposes (see 2.2),  $[\text{ZrO}]^{2+}[\text{UFP}]^{2-}$  is very interesting since the emission intensity of free umbelliferone (UF) in solution is considerably higher compared to the solid IOH-NPs (in suspension). Thus, UF release from the IOH-NPs, and thereupon, their dissolution can be directly monitored by fluorescence spectroscopy.<sup>[96]</sup> Whereas the UF release in aqueous suspensions at pH 7 and 37 °C is very slow, it can be significantly accelerated upon addition of acid phosphatase (Figure 21). Accordingly, the emission intensity rises continuously after phosphatase addition over a period of 10 h indicating the release of UF from the  $[\text{ZrO}]^{2+}[\text{UFP}]^{2-}$  IOH-NPs via hydrolytic cleavage of the P–O–C ester bond (Figure 21). On the one hand, this verifies the dissolution of the IOH-NPs, and on the other hand, this specific reaction can also serve as a

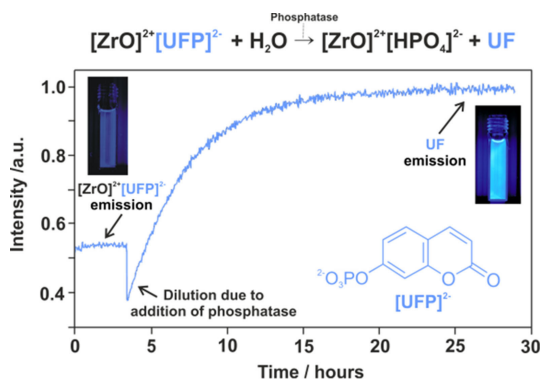


**Figure 21.** Monitoring the dissolution of  $[\text{ZrO}]^{2+}[\text{UFP}]^{2-}$  IOH-NPs: Fluorescence of aqueous suspensions prior (left cuvette) and after (right cuvette) the addition of acid phosphatase ( $\lambda_{\text{exc}} = 366$  nm), (modified reproduction from ref. [96]).

fluorescent probe of the presence of phosphatases.<sup>[96]</sup> To classify the timescale of the release reaction, it must be noticed that the hydrolysis of P–O–C ester bonds is particularly fast if the phosphate group is directly linked to an aromatic system  $\text{P–O–C}_{\text{aromatic}}$ .<sup>[97]</sup> In the case of aliphatic systems  $\text{P–O–C}_{\text{aliphatic}}$ , the release is significantly slower and moves on a timescale of several days.<sup>[35]</sup>

A second example to illustrate the dissolution of the IOH-NPs is  $[\text{ZrO}]^{2+}[\text{AAP}]^{2-}$ , containing the analgetic prodrug acetaminophen phosphate (AAP).<sup>[98]</sup> Here, the dissolution of the IOH-NPs and the release of acetaminophen (AA) were evaluated based on two different approaches. First, the carbon content of  $[\text{ZrO}]^{2+}[\text{AAP}]^{2-}$  was determined by EA (Figure 22a). Second, the

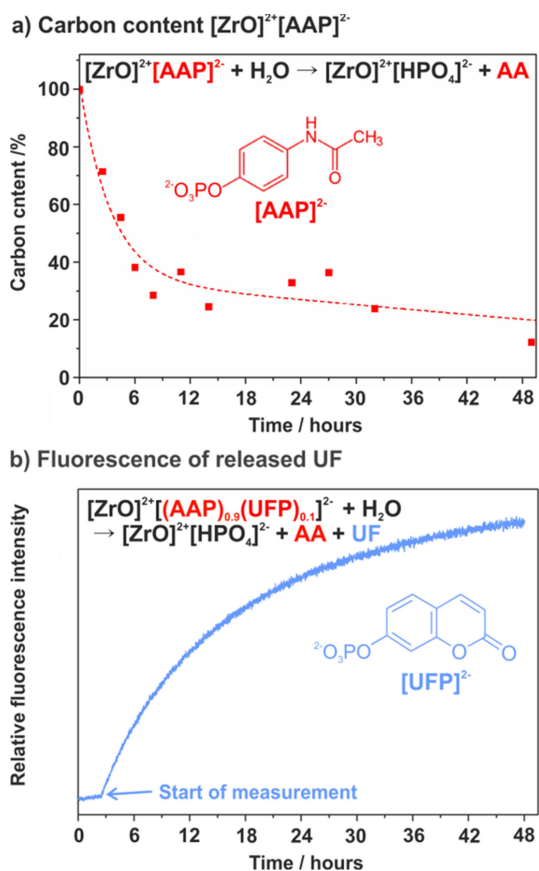


**Figure 22.** Monitoring the dissolution of  $[\text{ZrO}]^{2+}[\text{AAP}]^{2-}$  and  $[\text{ZrO}]^{2+}[(\text{AAP})_{0.9}(\text{UFP})_{0.1}]^{2-}$  IOH-NPs with: a) Determination of carbon content of the residual solid IOH-NPs via EA; b) Fluorescence detection of released UF (in solution) via fluorescence spectroscopy (48 h, pH 7, 25 °C), (modified reproduction from ref. [98]).

fluorescence of mixed-anion  $[\text{ZrO}]^{2+}[(\text{AAP})_{0.9}(\text{UFP})_{0.1}]^{2-}$  IOH-NPs containing 90 mol-% of  $[\text{AAP}]^{2-}$  and 10 mol-% of fluorescent  $[\text{UFP}]^{2-}$  was monitored.<sup>[98]</sup> Whereas EA is indicative for the AAP-related carbon content in the residual solid IOH-NPs, the fluorescence intensity refers to the released amounts of AA and UF in the solution. During the experiments, the IOH-NPs were continuously stirred in aqueous HEPES buffer at neutral pH and 25 °C. After certain periods of time, a defined aliquot of the suspension was extracted and centrifuged to obtain the IOH-

NPs and to perform EA.  $[\text{ZrO}]^{2+}[(\text{AAP})_{0.9}(\text{UFP})_{0.1}]^{2-}$  was treated similarly with repetitive measurements of the emission intensity (Figure 22b). Both measures – determination of carbon content and of emission intensity – indicate a continuous release of AA and UF with the as-expected exponential slope. Over 18 and 48 h, a total release of about 60 and 80% was observed, respectively. All in all, the release data stemming from carbon content and fluorescence detection show good coincidence.<sup>[98]</sup> Again, the timescale of release is comparably fast, since both AAP and UFP exhibit direct bonding of the phosphate group to an aromatic system ( $\text{P}-\text{O}-\text{C}_{\text{aromatic}}$ ).<sup>[97]</sup>

### 3.4. Drug Release and Delivery

Slow dissolution of IOH-NPs is not only relevant in terms of biocompatibility and biodegradability, but it is also the key to transfer the IOH-NP concept to drug release and drug delivery. Hence, the material platform and the feasibility of the IOH-NPs can become even broader.  $[\text{ZrO}]^{2+}[\text{AAP}]^{2-}$ , containing the analgetic prodrug acetaminophen phosphate, can be considered as a very first example for drug delivery and release that combines uncomplex synthesis in water with very high drug load of 68 wt-% AAP.<sup>[98]</sup>

Actually, the material concept has been already expanded to drug delivery and drug release, especially in the case of phosphate-based IOH-NPs. In this regard, numerous phosphate-functionalized pharmaceutical agents are available. Similar to the fluorescent  $[\text{ZrO}]^{2+}[\text{R}_{\text{Dye}}\text{OPO}_3]^{2-}$  IOH-NPs, a general composition  $[\text{ZrO}]^{2+}[\text{R}_{\text{Drug}}\text{OPO}_3]^{2-}$  can be derived for drug-containing IOH-NPs with a phosphate-functionalized pharmaceutical anion  $[\text{R}_{\text{Drug}}\text{OPO}_3]^{2-}$ .<sup>[99]</sup> Illustrative examples comprise, for instance,  $[\text{ZrO}]^{2+}[\text{FdUMP}]^{2-}$ ,  $[\text{ZrO}]^{2+}[\text{BMP}]^{2-}$  and  $[\text{ZrO}]^{2+}[\text{CLP}]^{2-}$  that contain the cytostatic agent 5'-fluoro-2'-deoxyuridine 5'-monophosphate (FdUMP),<sup>[35,100]</sup> the anti-inflammatory agent betamethasone phosphate (BMP),<sup>[35,101]</sup> and the antibiotic agent clindamycin phosphate (CLP) (Figure 23).<sup>[102]</sup> Similar to fluorescent IOH-NPs,  $[\text{ZrO}]^{2+}[\text{R}_{\text{Drug}}\text{OPO}_3]^{2-}$  also show excellent uptake into cells at high biocompatibility.<sup>[35,100–102]</sup> In difference

to  $[\text{ZrO}]^{2+}[\text{UFP}]^{2-}$  and  $[\text{ZrO}]^{2+}[\text{AAP}]^{2-}$  (see 3.3), the phosphate group in  $[\text{ZrO}]^{2+}[\text{FdUMP}]^{2-}$ ,  $[\text{ZrO}]^{2+}[\text{BMP}]^{2-}$  and  $[\text{ZrO}]^{2+}[\text{CLP}]^{2-}$  is linked to an aliphatic system ( $\text{P}-\text{O}-\text{C}_{\text{aliphatic}}$ ) that only shows slow hydrolysis and drug release (i.e. 5–10% release of total drug content after 48 h).<sup>[35,100–102]</sup>

The anti-proliferative potential of  $[\text{ZrO}]^{2+}[\text{FdUMP}]^{2-}$  (in suspension) with 75 wt-% load of active FdUMP was exemplarily shown on human mammary carcinoma cells and compared to non-active  $[\text{ZrO}]^{2+}[\text{UMP}]^{2-}$  IOH-NPs (in suspension) as negative control (UMP: uridine monophosphate) as well as to the clinically applied 5-FU (in solution) as positive control (5-FU: 5-fluorouracil).<sup>[100]</sup> Whereas  $[\text{ZrO}]^{2+}[\text{UMP}]^{2-}$  (negative control) had no effect on the cell viability, 5-FU (positive control) and  $[\text{ZrO}]^{2+}[\text{FdUMP}]^{2-}$  IOH-NPs show considerable cytostatic effects. Interestingly, the anti-proliferative activity of the  $[\text{ZrO}]^{2+}[\text{FdUMP}]^{2-}$  IOH-NPs is even higher than of 5-FU (positive control), although applied with identical concentration of the active agent.<sup>[100]</sup>  $[\text{ZrO}]^{2+}[\text{BMP}]^{2-}$  – as the second example – contains 81 wt-% of the glucocorticoid BMP and shows excellent anti-inflammatory response *in vitro* (MHS macrophages, primary mouse macrophages, human peripheral blood monocytes).<sup>[35,101]</sup> *In vivo* studies, furthermore, indicate a promising therapeutic efficiency in a mouse model of multiple sclerosis with a strongly increased cell-type specificity for macrophages compared to conventional free glucocorticoids (in solution).<sup>[101]</sup>  $[\text{ZrO}]^{2+}[\text{CLP}]^{2-}$  IOH-NPs, finally, represent a novel nanoparticle-based strategy to treat persisting and recurrent *Staphylococcus aureus*-caused infections.  $[\text{ZrO}]^{2+}[\text{CLP}]^{2-}$  also contains an extremely high amount of 82 wt-% of the clinically approved antibiotic clindamycin phosphate and shows high uptake at low toxicity. In comparison to the free drug in solution, most interestingly, the  $[\text{ZrO}]^{2+}[\text{CLP}]^{2-}$  IOH-NPs (in suspension) result in a 70 to 150-times higher drug uptake into cells, although both – free drug and IOH-NPs – were administered in identical concentrations.

Besides  $[\text{ZrO}]^{2+}[\text{FdUMP}]^{2-}$ ,  $[\text{ZrO}]^{2+}[\text{BMP}]^{2-}$  and  $[\text{ZrO}]^{2+}[\text{CLP}]^{2-}$  and their application for tumors, inflammation and infection, we could realize phosphate-based  $[\text{ZrO}]^{2+}[\text{R}_{\text{Drug}}\text{OPO}_3]^{2-}$  IOH-NPs with about 50 different pharmaceutical agents, which illustrates the feasibility of the concept as a general platform of materials. Drug delivery and drug release, however, are not a subject of this review and therefore only conceptually discussed as an additional option. Similar to  $[\text{ZrO}]^{2+}[(\text{HPO}_4)_{1-x}(\text{FMN})_x]^{2-}$  (see 2.2), the pharmaceutical anion  $[\text{R}_{\text{Drug}}\text{OPO}_3]^{2-}$  can be also partially exchanged by a fluorescent dye anion  $[\text{R}_{\text{Dye}}\text{OPO}_3]^{2-}$ . In order to maintain maximum drug load, the fluorescent dye anion is available only in low concentrations of 0.005 to 0.05 mol-%. Specifically, this results in  $[\text{ZrO}]^{2+}[(\text{FdUMP})_{0.95}(\text{ICG})_{0.05}]^{2-}$ ,  $[\text{ZrO}]^{2+}[(\text{BMP})_{0.95}(\text{FMN})_{0.05}]^{2-}$  or  $[\text{ZrO}]^{2+}[(\text{CLP})_{0.995}(\text{DUT})_{0.005}]^{2-}$ , which show drug release and which can be also detected via their fluorescence (see 2.2, 2.3, 3.1, Figure 23).<sup>[100–102]</sup>

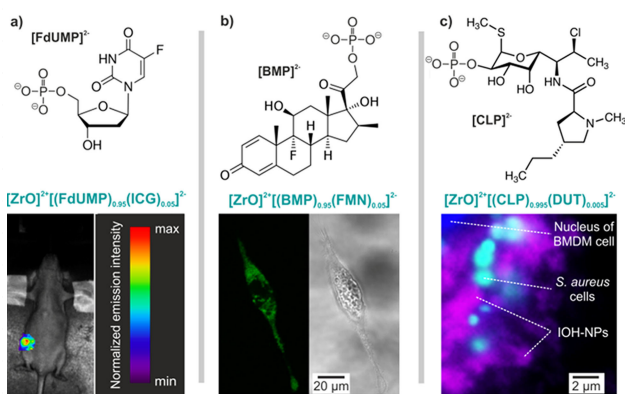


**Figure 23.** IOH-NPs for drug release with fluorescence labelling exemplarily shown for: a)  $[\text{ZrO}]^{2+}[(\text{FdUMP})_{0.95}(\text{ICG})_{0.05}]^{2-}$ , b)  $[\text{ZrO}]^{2+}[(\text{BMP})_{0.95}(\text{FMN})_{0.05}]^{2-}$ , and c)  $[\text{ZrO}]^{2+}[(\text{CLP})_{0.995}(\text{DUT})_{0.005}]^{2-}$  (modified reproduction from ref. [100–102]).

## 4. Conclusions

Phosphate- and sulfonate-based IOH-NPs with a general composition  $[\text{ZrO}]^{2+}[\text{R}_{\text{Dye}}\text{OPO}_3]^{2-}$ ,  $[\text{Ln}]^{3+}[\text{R}_{\text{Dye}}(\text{SO}_3)_n]^{n-}$ ,  $[\text{Ln}(\text{OH})]^{2+}[\text{R}_{\text{Dye}}(\text{SO}_3)_n]^{n-}$ , or  $[\text{LnO}]^+[\text{R}_{\text{Dye}}(\text{SO}_3)_n]^{n-}$  (Ln: lanthanide) are presented as a novel platform of functional nanoparticles for fluorescence detection and optical imaging. Specifically, the here discussed IOH-NPs include  $[\text{ZrO}]^{2+}[\text{HPO}_4]^{2-}$ ,  $[\text{ZrO}]^{2+}[(\text{HPO}_4)_{1-x}(\text{FMN})_x]^{2-}$ ,  $[\text{ZrO}]^{2+}[\text{FMN}]^{2-}$ ,  $[\text{ZrO}]^{2+}[\text{MFP}]^{2-}$ ,  $[\text{ZrO}]^{2+}[\text{RRP}]^{2-}$ ,  $[\text{ZrO}]^{2+}[\text{DUT}]^{2-}$ ,  $\text{La}^{3+}[\text{AMA}]^{3-}$ ,  $\text{Gd}^{3+}[\text{AMA}]^{3-}$ ,  $[\text{Gd}(\text{OH})]^{2+}_2[\text{CSB}]^{4-}$ ,  $[\text{Gd}(\text{OH})]^{2+}_2[\text{DB71}]^{4-}$ ,  $[\text{Gd}(\text{OH})]^{2+}[\text{NFR}]^{2-}$ ,  $[\text{Gd}(\text{OH})]^{2+}[\text{AR97}]^{2-}$ ,  $[\text{Gd}(\text{OH})]^{2+}_2[\text{EB}]^{4-}$ ,  $[\text{GdO}]^+[\text{ICG}]^-$ ,  $\text{Gd}_4^{3+}[\text{AIPCS}_4]_3^{4-}$ ,  $\text{La}_4^{3+}[\text{TPPS}_4]_3^{4-}$ ,  $[\text{ZrO}]^{2+}[\text{UFP}]^{2-}$ ,  $[\text{ZrO}]^{2+}[\text{AAP}]^{2-}$ ,  $[\text{ZrO}]^{2+}[\text{FdUMP}]^{2-}$ ,  $[\text{ZrO}]^{2+}[(\text{FdUMP})_{0.95}(\text{ICG})_{0.05}]^{2-}$ ,  $[\text{ZrO}]^{2+}[\text{BMP}]^{2-}$ ,  $[\text{ZrO}]^{2+}[(\text{BMP})_{0.95}(\text{FMN})_{0.05}]^{2-}$ ,  $[\text{ZrO}]^{2+}[\text{CLP}]^{2-}$ , and  $[\text{ZrO}]^{2+}[(\text{CLP})_{0.995}(\text{DUT})_{0.005}]^{2-}$ . Although already comprising a great number of compounds, these IOH-NPs stand as representatives for a much greater number of nanomaterials and an even broader platform of materials.

Besides the variability of the chemical composition, the IOH-NPs exhibit several features that differ from alternative fluorescent nanomaterials, including: *i*) Straightforward aqueous synthesis; *ii*) Low material complexity; *iii*) Extraordinarily high load of fluorescent dye and/or pharmaceutical drug (70–85 wt-% per nanoparticle); *iv*) Use of many approved fluorescent dyes; *v*) High biocompatibility and high biodegradability. All these aspects are highly relevant to medicine and clinical practice.

In addition to full-color emission, the IOH-NPs can feature even more functionalities. With  $\text{Gd}^{3+}$  as the inorganic cation, for instance, the IOH-NPs are magnetic and suitable for MRI. IOH-NPs such as  $[\text{GdO}]^+[\text{ICG}]^-$  are multimodal and applicable for OI (due to the emission of ICG), PAI (due to the absorption of ICG) and MRI (due to the paramagnetism of  $\text{Gd}^{3+}$ ). Moreover, IOH-NPs like  $\text{Gd}_4^{3+}[\text{AIPCS}_4]_3^{4-}$  or  $\text{La}_4^{3+}[\text{TPPS}_4]_3^{4-}$  show photo-induced ROS generation (singlet oxygen) and become suitable for photodynamic therapy. Finally, the phosphate- and/or sulfonate-based fluorescent anion can be replaced by pharmaceutical anions to realize IOH-NPs showing drug delivery and drug release. All these different features can be available in a single IOH-NP by combining two or more functional organic anions. All in all, the combination of inorganic cations and functional organic anions, like from a construction kit, allows realizing multimodal and multifunctional IOH-NPs with many more compositions and functions, which, in fact, is the most relevant feature and advantage of the IOH-NPs.

## Acknowledgements

The authors are grateful to additional partners from biology and medicine for excellent scientific cooperation, including Prof. U. Schaible, Research Center Borstel (tuberculosis); Prof. S. Boretius, Leibniz Institute of Primate Research Göttingen (MRI); Prof. T. Lammers, RWTH Aachen University Clinic (OI, PAI); Prof. I. Hilger, University Hospital Jena (MRI, magnetothermal heating); Prof. H. Garritsen, University Hospital Braunschweig (allergy). C.F. is grateful to Henriette Gröger and Nicole Klaassen for

accurate preparation and reproduction of IOH-NP samples. The authors acknowledge the German Research Society (DFG) for funding and equipment. Moreover, this work was supported by the DFG Research Training Group 2039 and the DFG graduate School “Karlsruhe School of Optics and Photonics (KSOP)” at the KIT, as well as by the German Federal Ministry of Education and Research (BMBF) within the joint research project ANTI-TB. Finally, M.K. acknowledges the Studienstiftung des deutschen Volkes for scholarship.

## Conflict of Interest

The authors declare no conflict of interest.

**Keywords:** inorganic-organic hybrids • phosphates • sulfonates • fluorescence • imaging

- a) D. Jin, P. Xi, B. Wang, L. Zhang, J. Enderlein, A. M. van Oijen, *Nat. Methods* **2018**, *15*, 1; b) E. B. Ehlerding, P. Grodzinski, W. Cai, C. H. Liu, *ACS Nano* **2018**, *12*, 2106; c) X. Zhao, C.-X. Yang, L.-G. Chen, X.-P. Yan, *Nat. Commun.* **2017**, *8*, 14998; d) T. K. Hill, A. M. Mohs, *Wiley Interdiscip. Rev. Nanomed. Nanobiotechnol.* **2016**, *8*, 498.
- a) K. Y. Zhang, Q. Yu, H. Wei, S. Liu, Q. Zhao, W. Huang, *Chem. Rev.* **2018**, *118*, 1770; b) J. Huang, N. Gretz, *ChemistryOpen* **2017**, *6*, 456; c) S. M. Ng, M. Koneswaran, R. Narayanaswamy, *RSC Adv.* **2016**, *6*, 21624; d) L. Bu, B. Shen, Z. Cheng, *Adv. Drug Delivery Rev.* **2014**, *76*, 21; e) O. S. Wolfbeis, *Chem. Soc. Rev.* **2015**, *44*, 4743; f) J. Yao, M. Yang, Y. Duan, *Chem. Rev.* **2014**, *114*, 6130; g) M. J. Ruedas-Rama, J. D. Walters, A. Orte, E. A. H. Hall, *Anal. Chim. Acta* **2012**, *751*, 1.
- a) T. Farncombe, K. Iniewski, *Medical Imaging: Technology and Applications*, CRC Press, Boca Raton, **2017**; b) A. G. Rockall, A. Hatrick, P. Armstrong, M. Wastie, *Diagnostic Imaging*, 7<sup>th</sup> Edition, Wiley, Chichester, **2013**; c) M. A. Anastasio, P. J. La Riviere, *Emerging Imaging Technologies in Medicine*, CRC Press, Boca Raton, **2012**.
- a) C. Kinnear, T. L. Moore, L. Rodriguez-Lorenzo, B. Rothen-Rutishauser, A. Petri-Fink, *Chem. Rev.* **2017**, *117*, 11476; b) M. Karimi, P. Sahandi Zangabad, S. Baghaee-Ravari, M. Ghazadeh, H. Mirshekari, M. R. Hamblin, *J. Am. Chem. Soc.* **2017**, *139*, 4584; c) K. Ulbrich, K. Hola, V. Šubr, A. Bakandritsos, J. Tuček, R. Zbořil, *Chem. Rev.* **2016**, *116*, 5338; d) P. T. Wong, S. K. Choi, *Chem. Rev.* **2015**, *115*, 3388.
- a) N. Zhang, M. Li, X. Sun, H. Jia, W. Liu, *Biomaterials* **2018**, *159*, 25; b) B. A. Kairdorf, X. Qian, S. Nie, *Anal. Chem.* **2017**, *89*, 1015; c) J. G. Fujimoto, D. Farkas, *Biomedical Optical Imaging*, Oxford University Press, Oxford, **2009**; d) K. M. Marks, G. P. Nolan, *Nat. Methods* **2006**, *3*, 591.
- a) H.-K. Kim, G. H. Lee, Y. Chang, *Future Med. Chem.* **2018**, *10*, 639; b) P. Verwilst, S. Park, B. Yoon, J. S. Kim, *Chem. Soc. Rev.* **2015**, *44*, 1791.
- B. M. Yeh, P. F. FitzGerald, P. M. Edic, J. W. Lambert, R. E. Colborn, M. E. Marino, P. M. Evans, J. C. Roberts, Z. J. Wang, M. J. Wong, *Adv. Drug Delivery Rev.* **2017**, *113*, 201.
- a) P. Bennett, U. D. Oza, *Diagnostic Imaging: Nuclear Medicine*, Elsevier, Amsterdam **2015**; b) T. Krüwel, D. Nevoltris, J. Bode, C. Dullin, D. Baty, P. Chames, F. Alves, *Sci. Rep.* **2016**, *6*, 21834.
- a) J. Y. J. Kim, S. Park, C. Lee, C. Kim, *ChemNanoMat* **2016**, *2*, 156; b) S. Kunjachan, J. Ehling, G. Storm, F. Kiessling, T. Lammers, *Chem. Rev.* **2015**, *115*, 10907; c) L. Nie, X. Chen, *Chem. Soc. Rev.* **2014**, *43*, 7132.
- a) S. K. Sun, H. F. Wang, X. P. Yan, *Acc. Chem. Res.* **2018**, *51*, 1131; b) G. Feng, B. Liu, *Acc. Chem. Res.* **2018**, *51*, 1404; c) S. K. Pahari, S. Olszakier, I. Kahn, L. Amirav, *Chem. Mater.* **2018**, *30*, 775; d) J.-Y. Zhao, G. Chen, Y.-P. Gu, R. Cui, Z.-L. Zhang, Z.-L. Yu, B. Tang, Y.-F. Zhao, D.-W. Pang, *J. Am. Chem. Soc.* **2016**, *138*, 1893; e) T. Shen, Y. Zhang, A. M. Kirillov, B. Hu, C. Shan, W. Liu, Y. Tang, *J. Mater. Chem. B* **2016**, *4*, 7832; f) Q. Sun, Q. You, J. Wang, L. Liu, Y. Wang, Y. Song, Y. Cheng, S. Wang, F. Tao, N. Li, *ACS Appl. Mater. Interfaces* **2018**, *10*, 1963; g) T. Nakamura, F. Sugihara, H. Matsushita, Y. Yoshioka, S. Mizukami, K. Kikuchi, *Chem. Sci.* **2015**, *6*, 1986; h) G. Song, C. Liang, H. Gong, M. Li, X. Zheng, L. Cheng, K. Yang, X. Jiang, Z. Liu, *Adv. Mater.* **2015**, *27*, 6110; i) E. Doolittle, P. M. Peiris, G.

- Doron, A. Goldberg, S. Tucci, S. Rao, S. Shah, M. Sylvestre, P. Govender, O. Turan, *ACS Nano* **2015**, *9*, 8012.
- [11] a) R. C. Somers, M. G. Bawendi, D. G. Nocera, *Chem. Soc. Rev.* **2007**, *36*, 579; b) X. Michalet, F. F. Pinaud, L. A. Bentolila, J. M. Tsay, S. Doose, J. J. Li, G. Sundaresan, A. M. Wu, S. S. Gambhir, S. Weiss, *Science* **2005**, *307*, 538.
- [12] a) G. R. Tan, M. Wang, C. Y. Hsu, N. Chen, Y. Zhang, *Adv. Opt. Mater.* **2016**, *4*, 984; b) W. Zheng, P. Huang, D. Tu, E. Ma, H. Zhu, X. Chen, *Chem. Soc. Rev.* **2015**, *44*, 1379; c) L.-D. Sun, Y.-F. Wang, C.-H. Yan, *Acc. Chem. Res.* **2014**, *47*, 1001; d) Y. Liu, D. Tu, H. Zhuab, X. Chen, *Chem. Soc. Rev.* **2013**, *42*, 6924.
- [13] a) A. Reisch, A. S. Klymchenko, *Small* **2016**, *12*, 1968; b) H.-S. Peng, D. T. Chiu, *Chem. Soc. Rev.* **2015**, *44*, 4699; c) K. Li, B. Liu, *Chem. Soc. Rev.* **2014**, *43*, 6570; d) C. Wu, D. T. Chiu, *Angew. Chem. Int. Ed.* **2013**, *52*, 3086; e) I. Johnson (Ed.), *Molecular Probes Handbook: A Guide to Fluorescent Probes and Labeling Technologies*, Life Technologies Corporation, Darmstadt, **2010**.
- [14] a) K. D. Wegner, N. Hildebrandt, *Chem. Soc. Rev.* **2015**, *44*, 4792; b) F. Ramos-Gomes, J. Bode, A. Sukhanova, S. V. Bozrova, M. Saccomano, M. Mitkovski, J. E. Krueger, A. K. Wege, W. Stuehmer, P. S. Samokhvalov *Sci. Rep.* **2018**, *8*, 4595.
- [15] S. Zhu, S. Tang, J. Zhang, B. Yang, *Chem. Commun.* **2012**, *48*, 4527.
- [16] O. Chen, J. Zhao, V. P. Chauhan, J. Cui, C. Wong, K. D. Harris, H. Wei, H.-S. Han, D. Fukumura, R. K. Jain, M. G. Bawendi, *Nat. Mater.* **2013**, *12*, 445.
- [17] a) K. J. McHugh, L. Jing, A. M. Behrens, S. Jayawardena, W. Tang, M. Gao, R. Langer, A. Jaklenec, *Adv. Mater.* **2018**, *30*, 1706356; b) N. Erathodiyil, J. Y. Ying, *Acc. Chem. Res.* **2011**, *44*, 925; c) I. L. Medintz, H. T. Uyeda, E. R. Goldman, H. Mattoussi, *Nat. Mater.* **2005**, *4*, 435; d) H. Zhang, D. Yee, C. Wang, *Nanomedicine* **2008**, *3*, 83.
- [18] a) Y.-P. Gu, R. Cui, Z.-L. Zhang, Z.-X. Xie, D.-W. Pang, *J. Am. Chem. Soc.* **2012**, *134*, 79; b) Y. He, Y. Zhong, Y. Su, Y. Lu, Z. Jiang, F. Peng, T. Xu, S. Su, Q. Huang, C. Fan, *Angew. Chem.* **2011**, *123*, 5813; *Angew. Chem. Int. Ed.* **2011**, *50*, 5695; c) S. Santra, H. Yang, P. H. Holloway, J. T. Stanley, R. A. Mericle, *J. Am. Chem. Soc.* **2005**, *127*, 1656.
- [19] a) V. Sharma, P. Tiwari, S. M. Mobin, *J. Mater. Chem. B* **2017**, *5*, 8904; b) N. L. Teradal, R. Jelinek, *Adv. Healthcare Mater.* **2017**, *6*, 1700574; c) C. Ding, A. Zhu, Y. Tian, *Acc. Chem. Res.* **2014**, *47*, 20.
- [20] M. Haase, H. Schäfer, *Angew. Chem.* **2011**, *123*, 5928; *Angew. Chem. Int. Ed.* **2011**, *50*, 5808.
- [21] a) D. Ding, K. Li, B. Liu, B. Z. Tang, *Acc. Chem. Res.* **2013**, *46*, 2441; b) G. Booth, *Dyes-General Survey*. Wiley-VCH, Weinheim, **2000**.
- [22] a) V. Martinez, M. Henary, *Chem. Eur. J.* **2016**, *22*, 13764; b) U. Resch-Genger, M. Grabolle, S. Cavaliere-Jaricot, R. Nitschke, T. Nann, *Nat. Methods* **2008**, *5*, 763.
- [23] a) M. J. Schnermann, *Nature* **2017**, *551*, 176; b) L. Yuan, W. Lin, K. Zheng, L. He, W. Huang, *Chem. Soc. Rev.* **2013**, *42*, 622; c) M. Beija, C. A. M. Afonso, J. M. G. Martinho, *Chem. Soc. Rev.* **2009**, *38*, 2410.
- [24] a) M. Zhang, L. Zhang, Y. Chen, L. Li, Z. Su, C. Wang, *Chem. Sci.* **2017**, *8*, 8067; b) Q. Lei, W.-X. Qiu, J.-J. Hu, P.-X. Cao, C.-H. Zhu, H. Cheng, X.-Z. Zhang, *Small* **2016**, *12*, 4286; c) M. Montalti, L. Prodi, E. Rampazzo, N. Zaccheroni, *Chem. Soc. Rev.* **2014**, *43*, 4243; d) N. Zhang, E. Ding, X. Feng, Y. Xu, H. Cai, *Colloids Surf. B* **2012**, *89*, 133; e) D. Knopp, D. Tang, R. Niessner, *Anal. Chim. Acta* **2009**, *647*, 14; f) H. S. Muddana, T. T. Morgan, J. H. Adair, P. J. Butler, *Nano Lett.* **2009**, *9*, 1559; g) A. A. Burns, J. Vider, H. Ow, E. Herz, O. Penate-Medina, M. Baumgart, S. M. Larson, U. Wiesner, M. Bradbury, *Nano Lett.* **2009**, *9*, 442; h) E. I. Altinoglu, T. J. Russin, J. M. Kaiser, B. M. Barth, P. C. Eklund, M. Kester, J. H. Adair, *ACS Nano* **2008**, *2*, 2075; i) J. E. Fuller, G. T. Zugates, L. S. Ferreira, H. Ow, N. N. Nguyen, U. Wiesner, R. S. Langer, *Biomaterials* **2008**, *29*, 1526.
- [25] a) C. He, D. Liu, W. Lin, *Chem. Rev.* **2015**, *115*, 11079; b) H. Tan, C. Ma, L. Chen, F. Xu, S. Chen, L. Wang, *Sens. Actuators B* **2014**, *190*, 621; c) R. C. Huxford-Phillips, K. E. DeKrafft, W. S. Boyle, D. Liu, W. Lin, *Chem. Sci.* **2012**, *3*, 198; d) J. Della Rocca, D. Liu, W. Lin, *Acc. Chem. Res.* **2011**, *44*, 957; e) A. M. Spokoiny, D. Kim, A. Sumrein, C. A. Mirkin, *Chem. Soc. Rev.* **2009**, *38*, 1218.
- [26] a) A. Reisch, A. S. Klymchenko, *Small* **2016**, *12*, 1968. b) C. Zheng, M. Zheng, P. Gong, D. Jia, P. Zhang, B. Shi, Z. Sheng, Y. Ma, L. Cai, *Biomaterials* **2012**, *33*, 5603. c) G. A. Hughes, *Nanomedicine* **2005**, *1*, 22.
- [27] a) H. Hu, C. Xiao, H. Wu, Y. Li, Q. Zhou, Y. Tang, C. Yu, X. Yang, Z. Li, *ACS Appl. Mater. Interfaces* **2017**, *9*, 42225; b) L.-j. Chen, C.-X. Yang, X.-P. Yan, *Anal. Chem.* **2017**, *89*, 6936; c) Y. Huang, E. Hemmer, F. Rosei, F. Vetrone, *J. Phys. Chem. B* **2016**, *120*, 4992; d) Z. Shen, D. T. Loe, J. K. Awino, M. Kröger, J. L. Rouge, Y. Li, *Nanoscale* **2016**, *8*, 14821; e) D. Goyard, T. C. Shiao, N. L. Fraleigh, H.-Y. Vu, H. Lee, F. Diaz-Mitoma, H.-T. Le, R. Roy, *J. Mater. Chem. B* **2016**, *4*, 4227; f) K. K. Ng, M. Takada, K. Harmatys, J. Chen, G. Zheng, *ACS Nano* **2016**, *10*, 4092; g) T. Hu, H. Cao, C. Yang, L. Zhang, X. Jiang, X. Gao, F. Yang, G. He, X. Song, A. Tong, *Appl. Mater. Interfaces* **2016**, *8*, 6586; h) S. Parveen, R. Misra, S. K. Sahoo, *Nanomedicine* **2012**, *8*, 147.
- [28] P. Pallavicini, Y. A. Diaz-Fernandez, L. Pasotti, *Coord. Chem. Rev.* **2009**, *253*, 2226.
- [29] Z. Cheng, A. Al Zaki, J. Z. Hui, V. R. Muzykantov, A. Tsourkas, *Science* **2012**, *338*, 903.
- [30] M. Roming, C. Feldmann, *Patent application* DE 102008009541.9.
- [31] J. M. Berg, J. L. Tymoczko, G. J. Gatto, L. Stryer, *Biochemistry*, 8<sup>th</sup> Edition, Freeman, New York, **2015**.
- [32] E. Schweda, *Jander/Blasius: Anorganische Chemie 1*, 18<sup>th</sup> Edition, Hirzel, Stuttgart, **2016**, p. 447.
- [33] J. Strähle, E. Schweda, *Jander/Blasius: Einführung in das anorganisch-chemische Praktikum*, 14<sup>th</sup> Edition, Hirzel, Stuttgart, **2016**, p. 112.
- [34] M. Roming, H. Lünsdorf, K. E. J. Dittmar, C. Feldmann, *Angew. Chem.* **2010**, *122*, 642; *Angew. Chem. Int. Ed.* **2010**, *49*, 632.
- [35] J. G. Heck, J. Napp, S. Simonato, J. Möllmer, M. Lange, H. R. Reichardt, R. Staudt, F. Alves, C. Feldmann, *J. Am. Chem. Soc.* **2015**, *137*, 7329.
- [36] M. Roming, C. Feldmann, *Patent application* WO 2009/100800 A1, EP 2179006 A1, US 12/867,348.
- [37] a) H. Tan, C. Ma, L. Chen, F. Xu, S. Chen, L. Wang, *Sens. Actuators B* **2014**, *190*, 621; b) C. Ma, H. Tan, L. Chen, Y. Song, F. Xu, S. Chen, L. Wang, *Sens. Actuators B* **2014**, *202*, 683; c) D. Liu, C. He, C. Y. Poon, W. Lin, *J. Mater. Chem. B* **2014**, *2*, 8249; d) D. Liu, S. A. Kramer, R. C. Huxford-Phillips, S. Wang, J. Della Rocca, W. Lin, *Chem. Commun.* **2012**, *48*, 2668.
- [38] D. K. Packham, H. S. Rasmussen, P. T. Lavin, M. A. El-Shahawy, S. D. Roger, G. Block, W. Qunibi, P. Pergola, B. Singh, *Eng. Med.* **2015**, *372*, 222.
- [39] E. S. Abrutyn, *Cosmet. Toiletries* **2011**, *126*, 780.
- [40] H. Du, R.-C. A. Fuh, J. Li, L. A. Corkan, J. S. Lindsey, *Photochem. Photobiol.* **1998**, *68*, 141.
- [41] S. Ghosh, A. Sharma, G. Talukder, *Biol. Trace Elem. Res.* **1992**, *35*, 247.
- [42] V. K. LaMer, R. H. Dinegar, *J. Am. Chem. Soc.* **1950**, *72*, 4847.
- [43] A. Clearfield, R. H. Blessing, J. A. Stynes, *J. Inorg. Nucl. Chem.* **1968**, *30*, 2249.
- [44] a) X. Cai, A. Bandla, D. Mao, G. Feng, W. Qin, L.-d. Liao, N. Thakor, B. Z. Tang, B. Liu, *Adv. Mater.* **2016**, *28*, 8760; b) M. E. Davis, *MRS Bull.* **2012**, *37*, 828; c) R. Weisleder, *Nat. Biotechnol.* **2001**, *19*, 316.
- [45] a) K. Rurack, M. Spieles, *Anal. Chem.* **2011**, *83*, 1232; b) K. Kolmakov, V. Belov, J. Bierwagen, C. Ringemann, V. Mueller, C. Eggeling, S. W. Hell, *Chem. Eur. J.* **2010**, *16*, 158.
- [46] a) J. E. Hulla in: *Hayes' Principles and Methods of Toxicology* (Eds.: A. W. Hayes, C. L. Kruger), 6<sup>th</sup> Edition, CRC Press, Boca Raton, **2014**, pp. 825; b) H. Greim, *The MAK collection for occupational health and safety*, Vol. 12, Wiley-VCH, Weinheim, **2006**, pp. 223.
- [47] R. D. Shannon, *Acta Crystallogr. Sect. A* **1976**, *32*, 751.
- [48] M. Poß, J. Napp, O. Niehaus, R. Pöttgen, F. Alves, C. Feldmann, *J. Mater. Chem. C* **2015**, *3*, 3860.
- [49] European Food Safety Authority, *EFSA J.* **2010**, *8*, 1649.
- [50] a) H. Dong, Y.-C. Chen, C. Feldmann, *Green Chem.* **2015**, *17*, 4107; b) R. Witter, M. Roming, C. Feldmann, A. S. Ulrich, *J. Colloid Interface Sci.* **2013**, *390*, 250.
- [51] a) S. Abbas, I. Yadav, S. Kumar, V. K. Aswal, J. Kohlbrecher, *Chem. Phys. Lett.* **2017**, *675*, 124; b) M. A. Brown, Z. Abbas, A. Kleibert, R. G. Green, A. Goel, S. May, T. M. Squires, *Phys. Rev. X* **2016**, *6*, 11007.
- [52] G. Chen, F. Song, X. Wang, S. Sun, J. Fan, X. Peng, *Dyes Pigm.* **2012**, *93*, 1532.
- [53] H. Ow, D. R. Larson, M. Srivastava, B. A. Baird, W. W. Webb, U. Wiesner, *Nano Lett.* **2005**, *5*, 113.
- [54] S. Bhattacharyya, S. Prashanthi, P. R. Bangal, A. Patra, *J. Phys. Chem. C* **2013**, *117*, 26750.
- [55] a) T.-H. Shin, Y. Choi, S. Kim, J. Cheon, *Chem. Soc. Rev.* **2015**, *44*, 4501; b) W. J. Mulder, G. J. Strijkers, G. A. van Tilborg, A. W. Griffioen, K. Nicolay, *NMR Biomed.* **2006**, *19*, 142.
- [56] a) E. J. Rummeny, E. Reimer, W. Heindel, *Ganzkörper-MR-Tomographie* (Ed: U. Mödder), Thieme, Stuttgart, New York, **2011**; b) C. A. Chang, L. C. Francesconi, M. F. Malley, K. Kumar, J. Z. Gougoutas, M. F. Tweedle, D. W. Lee, L. J. Wilson, *Inorg. Chem.* **1993**, *32*, 3501.
- [57] I. N. Mbawuiki, H. B. Herscovitz, *J. Leukocyte Biol.* **1989**, *46*, 119.
- [58] M. Poß, E. Zittel, U. Schepers, C. Feldmann, *Bioconjugate Chem.* **2018**, DOI:10.1021/acs.bioconjchem.8b00423.

- [59] A. McLintock, C. A. Cunha-Matos, M. Zagnoni, O. R. Millington, A. W. Wark, *ACS Nano* **2014**, *8*, 8600.
- [60] a) Z. Li, P. Liu, T. Yang, Y. Sun, Q. You, J. Li, Z. Wang, B. Han, *J. Biomater. Appl.* **2016**, *30*, 1552; b) T. B. Bemenderfer, J. S. Harris, K. W. Condon, M. A. Kacena, *Methods Mol. Biol.* **2014**, *1130*, 123; c) M. Frank, R. Dapson, T. Wickersham, J. Kiernan, *Biotech. Histochem.* **2007**, *82*, 35; d) M. A. Thomas, B. Lemmer, *Brain Res. Protoc.* **2005**, *14*, 107; e) A. G. Chowdhury, B. Dasgupta, H. N. Ray, *Nature* **1955**, *176*, 701.
- [61] a) W. Y. Jang, B.-R. Lee, J. Jeong, Y. Sung, M. Choi, P. Song, H. Kim, S. Jang, H. Kim, K.-I. Joo, *Brain Res.* **2017**, *1654*, 55; b) L. Xu, F. Cao, F. Xu, B. He, Z. Dong, M. Koval, *PLoS One* **2015**, *10*, e0122744; c) A. Valigurová, G. G. Paskerova, A. Diakin, M. Kováčiková, T. G. Simdyanov, T. Spielmann, *PLoS One* **2015**, *10*, e0125063; d) N. Sándor, F. R. Walter, A. Bocsik, P. Sántha, B. Schilling-Tóth, V. Léner, Z. Varga, Z. Kahán, M. A. Deli, G. Sáfrány, *PLoS One* **2014**, *9*, e112397.
- [62] a) B. T. Roller, J. M. Munson, B. Brahma, P. J. Santangelo, S. B. Pai, R. V. Bellamkonda, *Drug Delivery Transl. Res.* **2015**, *5*, 116; b) Y. Cui, J. Yu, S. Feng, *Talanta* **2014**, *130*, 536; c) S. N. Tabatabaei, H. Girouard, A.-S. Carret, S. Martel, *J. Controlled Release* **2015**, *206*, 49; d) S. J. Isak, E. M. Eyring, J. D. Spikes, P. A. Meekins, *J. Photochem. Photobiol. A* **2000**, *134*, 77.
- [63] a) K. M. Marks, G. P. Nolan, *Nat. Methods* **2006**, *3*, 591. b) A. N. Butkevich, G. Y. Mitronova, S. C. Sidenstein, J. L. Klocke, D. Kamin, D. N. H. Meineke, E. D'Este, P. T. Kraemer, J. G. Danzl, V. N. Below, *Angew. Chem.* **2016**, *128*, 3350; *Angew. Chem. Int. Ed.* **2016**, *55*, 3290.
- [64] M. Snehalatha, C. Ravikumar, N. Sekar, V. S. Jayakumar, I. H. Joe, *Raman* **2008**, *39*, 928.
- [65] J. Paul, J. R. Ebdon, *Phosphorus-based flame retardants in: Fire Retardancy of Polymeric Materials* (Eds.: C. A. Wilkie, A. B. Morgan), 2<sup>nd</sup> Edition, **2010**, pp. 107-125.
- [66] a) D. Gui, T. Zheng, J. Xie, Y. Cai, Y. Wang, L. Chen, J. Diwu, Z. Chai, S. Wang, *Inorg. Chem.* **2016**, *55*, 12508; b) S. Bruque, M. A. G. Aranda, E. R. Losilla, P. Olivera-Pastor, M. Maireles-Torres, *Inorg. Chem.* **1995**, *34*, 893; c) L. Sedláčková, V. Pekárek, *J. Less-Common Met.* **1966**, *10*, 130.
- [67] a) R. Silbernagel, C. H. Martin, A. Clearfield, *Inorg. Chem.* **2016**, *55*, 1651. b) A. Donnadio, M. Nocchetti, F. Costantino, M. Taddei, M. Casciola, F. Lisboa, R. Vivani, *Inorg. Chem.* **2014**, *53*, 13220. c) A. Donnadio, M. Pica, S. Subianto, D. J. Jones, P. Cojocar, M. Casciola, *ChemSusChem* **2014**, *7*, 2176. d) L. M. Liu, G. Y. Lu, L. P. Jiang, J. J. Zhu, *J. Solid State Chem.* **2014**, *215*, 74. e) M. Pica, A. Donnadio, R. D'Amato, D. Capitani, M. Taddei, M. Casciola, *Inorg. Chem.* **2014**, *53*, 2222.
- [68] a) Y. Zhang, X. Zeng, X. Lai, H. Li, *RSC Adv.* **2018**, *8*, 111; b) F. Carosio, J. Alongi, G. Malucelli, *J. Mater. Chem.* **2011**, *21*, 10370.
- [69] M. Poß, R. J. Tower, J. Napp, L. C. Appold, T. Lammers, F. Alves, C.-C. Glüer, S. Boretius, C. Feldmann, *Chem. Mater.* **2017**, *29*, 3547.
- [70] M. Poß, H. Gröger, C. Feldmann, *Chem. Commun.* **2018**, *54*, 1245.
- [71] a) C. Giraudeau, A. Moussaron, A. Stallivieri, S. Mordon, C. Frochot, *Curr. Med. Chem.* **2014**, *21*, 1871; b) Z. Sheng, D. Hu, M. Xue, M. He, P. Gong, L. Cai, *Nano-Micro Lett.* **2013**, *5*, 145; c) R. Hua, L. Liu, X. Wang, L. Chen, Y. Zheng, *PLoS One* **2013**, *8*, e83494; d) S. T. Proulx, P. Luciani, S. Derzi, M. Rinderknecht, V. Mumprecht, J.-C. Leroux, M. Detmar, *Cancer Res.* **2010**, *70*, 7053; e) G. C. Taichman, P. J. Hendry, W. J. Keon, *Texas Heart Institute* **1987**, *14*, 133.
- [72] M. S. Schreiner, L. G. Leksell, G. R. Neufeld, *J. Clin. Monitoring* **1989**, *5*, 236.
- [73] A. Ashokan, G. S. Gowd, V. H. Somasundaram, A. Bhupathi, R. Peethambaran, A. K. K. Unni, S. Palaniswamy, S. V. Nair, M. Koyakutty, *Biomaterials* **2013**, *34*, 7143.
- [74] a) J. H. Park, J. H. Choi, J. H. Son, S. J. Hwang, H. Seo, I.-K. Kang, M. Park, J. Kim, D. C. Hyun, *Polymer* **2018**, *135*, 211; b) Y. Yu, Z. Zhang, Y. Wang, H. Zhu, F. Li, Y. Shen, S. Guo, *Acta Biomater.* **2017**, *59*, 170; c) H. K. Yoon, A. Ray, Y.-E. K. Lee, G. Kim, X. Wang, R. Kopelman, *J. Mater. Chem. B* **2013**, *11*, 1; d) M. Zheng, C. Yue, Y. Ma, P. Gong, P. Zhao, C. Zheng, Z. Sheng, P. Zhang, Z. Wang, L. Cai, *ACS Nano* **2013**, *7*, 2056; e) T. T. Morgan, H. S. M. Erhan, I. Altinoglu, S. M. Rouse, A. Tabakovic, T. Tabouillot, T. J. Russin, S. S. Shanmugavelandy, P. J. Butler, P. K. Eklund, J. K. Yun, M. Kester, J. H. Adair, *Nano Lett.* **2008**, *8*, 4108.
- [75] a) S. Guan, Y. Weng, M. Li, R. Liang, C. Sun, X. Qu, S. Zhou, *Nanoscale* **2017**, *9*, 10367; b) C. Li, R. Liang, R. Tian, S. Guan, D. Yan, J. Luo, M. Wei, D. G. Evans, X. Duan, *RSC Adv.* **2016**, *6*, 16608; c) S. Guan, R. Liang, C. Li, D. Yan, M. Wei, D. G. Evans, X. Duan, *J. Mater. Chem. B* **2016**, *4*, 1331.
- [76] a) Y. Chao, P. P. Karmali, R. Mukthavaram, S. Kesari, V. L. Kouznetsova, I. F. Tsigelny, D. Simberg, *ACS Nano* **2013**, *7*, 4289; b) L. K. Bogart, A. Taylor, Y. Cesbron, P. Murray, R. Lévy, *ACS Nano* **2012**, *6*, 5961.
- [77] a) A. Hannah, G. Luke, K. Wilson, K. Homan, S. Emelianov, *ACS Nano* **2014**, *8*, 250; b) A. de La Zerda, Z. Liu, S. Bodapati, R. Teed, S. Vaithilingam, B. T. Khuri-Yakub, X. Chen, H. Dai, S. S. Gambhir, *Nano Lett.* **2010**, *10*, 2168; c) H. F. Zhang, K. Maslov, G. Stoica, L. V. Wang, *Nat. Biotechnol.* **2006**, *24*, 848.
- [78] M. Poß, E. Zittel, C. Seidl, A. Meschkov, L. Munoz, U. Schepers, C. Feldmann, *Adv. Funct. Mater.* **2018**, *28*, 1801074.
- [79] a) W. Zhang, W. Lai, R. Cao, *Chem. Rev.* **2017**, *117*, 3717; b) A. A. Ghogare, A. Greer, *Chem. Rev.* **2016**, *116*, 9994; c) W. Fan, P. Li, *Angew. Chem.* **2014**, *126*, 12397; *Angew. Chem. Int. Ed.* **2014**, *53*, 12201; d) M. Lian, Z. Li, Y. Cai, Q. Meng, Z. Gao, *Chem. Asian J.* **2012**, *7*, 2019; e) J. H. Zagal, S. Griveau, J. F. Silva, T. Nyokong, F. Bedioui, *Coord. Chem. Rev.* **2010**, *254*, 2755.
- [80] a) L. Jiang, C. R. R. Gan, J. Gao, X. J. Loh, *Small* **2016**, *12*, 3609; b) L. Fernández, V. I. Esteves, Á. Cunha, R. J. Schneider, J. P. C. Tomé, J. Porphyrins *Phthalocyanines* **2016**, *20*, 150; c) S. Zargari, R. Rahimi, A. Yousefi, *RSC Adv.* **2016**, *6*, 24218; d) J. Almeida, J. P. C. Tomé, Maria G. P. M. S. Neves, A. C. Tomé, J. A. S. Cavaleiro, Á. Cunha, L. Costa, M. A. F. Faustino, A. Almeida, *Photochem. Photobiol. Sci.* **2014**, *13*, 626.
- [81] a) J. M. Dabrowski, B. Pucelik, A. Regiel-Futyr, M. Brindell, O. Mazuryk, A. Kyzioł, G. Stochel, L. G. Arnaut, *Coord. Chem. Rev.* **2016**, *325*, 67; b) Y. Zhou, X. Liang, Z. Dai, *Nanoscale* **2016**, *8*, 12394; c) H. Abrahamse, M. R. Hamblin, *Biochem. J.* **2016**, *473*, 347; d) A. Oniszczuk, K. A. Wojtunik-Kulesza, T. Oniszczuk, K. Kasprzak, *Biomed. Pharmacother.* **2016**, *83*, 912; e) S. Singh, A. Aggarwal, Bhupathiraju, N. V. S. Dinesh, K. G. Arianna, K. Tiwari, C. M. Drain, *Chem. Rev.* **2015**, *115*, 10261; f) D. Dolmans, D. Fukumura, J. Rakesh, *Nat. Rev. Cancer* **2003**, *3*, 380.
- [82] a) T. Patrice, N. Brasseur *Sensitizers for PDT in Photodynamic Therapy, Vol. 2* (Ed.: T. Patrice), RSC Press, London, **2003**, pp. 105-118; b) U.S. Food and Drug Administration (FDA), *Approved Drug Products with Therapeutic Equivalence Evaluations*, 37<sup>th</sup> Edition, **2017**.
- [83] a) X.-S. Li, M.-R. Ke, W. Huang, C.-H. Ye, J.-D. Huang, *Chem. Eur. J.* **2015**, *21*, 3310; b) E. Ahmadi, A. Ramazani, A. Mashhadi-Malekzadeh, Z. Hamdi, Z. Mohamadnia, *Bull. Mater. Sci.* **2014**, *37*, 1101; c) E. S. Shibui, M. Hamada, N. Murase, V. Biju, *J. Photochem. Photobiol. C* **2013**, *15*, 53; d) M. L. Marin, L. Santos-Juanes, A. Arques, A. M. Amat, M. A. Miranda, *Chem. Rev.* **2012**, *112*, 1710; e) V. Latour, T. Pigot, P. Mocho, S. Blanc, S. Lacombe, *Catal. Today* **2005**, *101*, 359; f) S. Wang, R. Gao, F. Zhou, M. Selke, *J. Mater. Chem.* **2004**, *14*, 487; g) N. A. Kuznetsova, N. S. Gretsova, V. M. Derkacheva, O. L. Kaliya, E. A. Lukyanets, *J. Porphyrins Phthalocyanines* **2003**, *7*, 147.
- [84] a) A. Fraix, I. Manet, M. Ballestri, A. Guerrini, P. Dambruoso, G. Sotgiu, G. Varchi, M. Camerin, O. Coppellotti, S. Sortino, *J. Mater. Chem. B* **2015**, *3*, 3001; b) M. Trapani, A. Romeo, T. Parisi, M. T. Sciortino, S. Patané, V. Villari, A. Mazzaglia, *RSC Adv.* **2013**, *3*, 5607.
- [85] a) X.-g. Yi, J.-g. Huang, R.-h. Hu, Z.-g. Luo, *J. Porphyrins Phthalocyanines* **2015**, *19*, 1072; b) J. Demel, P. Kubát, F. Millange, J. Marrot, I. Čišarová, K. Lang, *Inorg. Chem.* **2013**, *52*, 2779.
- [86] F. Fernandez-Trillo, L. M. Grover, A. Stephenson-Brown, P. Harrison, P. M. Mendes, *Angew. Chem.* **2017**, *129*, 3188; *Angew. Chem. Int. Ed.* **2017**, *56*, 3142.
- [87] J. Mosinger, Z. Mička, *J. Photochem. Photobiol. A* **1997**, *107*, 77.
- [88] W. P. Helman, A. B. Ross, *J. Phys. Chem. Ref. Data* **1993**, *22*, 113.
- [89] a) J.-M. Hermann, *Appl. Catal. B* **2010**, *99*, 461; b) B. Ohtani, *Chem. Lett.* **2008**, *37*, 216; c) J.-M. Herrmann, *Catal. Today* **1999**, *53*, 115.
- [90] W. Fan, P. Huang, X. Chen, *Chem. Soc. Rev.* **2016**, *45*, 6488.
- [91] a) Y. Wang, Y. Xie, J. Li, Z.-H. Peng, Y. Sheinin, J. Zhou, D. Oupický, *ACS Nano* **2017**, *11*, 2227; b) D. Wang, T. Wang, J. Liu, H. Yu, S. Jiao, B. Feng, F. Zhou, Y. Fu, Q. Yin, P. Zhang, *Nano Lett.* **2016**, *16*, 5503; c) H. Gong, Y. Chao, J. Xiang, X. Han, G. Song, L. Feng, J. Liu, G. Yang, Q. Chen, Z. Liu, *Nano Lett.* **2016**, *16*, 2512; d) C. Liang, S. Diao, C. Wang, H. Gong, T. Liu, G. Hong, X. Shi, H. Dai, Z. Liu, *Adv. Mater.* **2014**, *26*, 5646.
- [92] K. Plaetzer, B. Krammer, J. Berlanda, F. Berr, T. Kiesslich, *Lasers Med. Sci.* **2009**, *24*, 259.
- [93] a) S. S. Lucky, K. C. Soo, Y. Zhang, *Chem. Rev.* **2015**, *115*, 1990; b) Y. Shen, A. J. Shuhendler, D. Ye, J.-J. Xu, H.-Y. Chen, *Chem. Soc. Rev.* **2016**, *45*, 6725; c) S. Wang, A. Bi, W. Zeng, Z. Cheng, *J. Mater. Chem. B* **2016**, *4*, 5331; d) L. Cheng, C. Wang, L. Feng, K. Yang, Z. Liu, *Chem. Rev.* **2014**, *114*, 10869.
- [94] M. C. Mione, N. S. Trede, *Dis. Model Mech.* **2010**, *3*, 517.
- [95] T. D. H. Bugg, *Introduction to Enzyme and Coenzyme Chemistry, 3<sup>rd</sup> Edition*, Wiley, Chichester, **2012**, pp. 77.
- [96] M. Roming, C. Feldmann, *Solid State Sci.* **2011**, *13*, 508.
- [97] J. B. Vincent, M. W. Crowder, B. A. Averill, *Trends Biochem. Sci.* **1992**, *17*, 105.

- [98] J. G. Heck, C. Feldmann, *J. Colloid Interface Sci.* **2016**, *481*, 69.
- [99] J. Heck, M. Poß, J. Napp, W. Stühmer, H. M. Reichardt, F. Alves, C. Feldmann, *Patent application* DE 102014004512.9, PCT/EP2015/000454, WO 2015144282, EP 3122756, CN 106660944, JP 2017513820, US 20170112948.
- [100] J. Napp, J. G. Heck, C. Feldmann, F. Alves, **2018**, in preparation.
- [101] a) E. Montes-Cobos, S. Ring, H. J. Fischer, J. G. Heck, J. Strauß, M. Schwaninger, S. D. Reichardt, C. Feldmann, F. Lühder, H. M. Reichardt, *J. Controlled Release* **2017**, *245*, 157; b) J. Napp, A. Markus, J. G. Heck, C. Dullin, W. Möbius, M. Koch, C. Feldmann, F. Alves, **2018**, in revision.
- [102] J. G. Heck, K. Rox, H. Luensdorf, T. Lueckerath, N. Klaassen, E. Medina, O. Goldmann, C. Feldmann, *ACS Omega* **2018**, *3*, 8589.

---

Manuscript received: July 5, 2018  
 Accepted Article published: September 19, 2018  
 Version of record online: ■ ■ , ■■■■

---

## FOCUS REVIEW

Extremely high dye contents (70–85 wt-%) are available in inorganic-organic hybrid nanoparticles (IOH-NPs) such as  $[\text{ZrO}]^{2+}[\text{R}_{\text{Dye}}\text{OPO}_3]^{2-}$ . They show intense emission, high photostability, high cell uptake at low toxicity, and they are also suitable for multimodal imaging, singlet-oxygen generation and drug delivery.



### Hybrid Materials

*B. L. Neumeier, M. Khorenko, Prof. Dr. F. Alves, Dr. O. Goldmann, Dr. J. Napp, Prof. Dr. U. Schepers, Prof. Dr. H. M. Reichardt, Prof. Dr. C. Feldmann\**

1 – 23

### Fluorescent Inorganic-Organic Hybrid Nanoparticles

